ASCA OBSERVATIONS OF SEYFERT 1 GALAXIES. II. RELATIVISTIC IRON Kα EMISSION

K. NANDRA,[1,2] I. M. GEORGE,[1,3] R. F. MUSHOTZKY,[1] T. J. TURNER,[1,3] AND T. YAQOOB[1,3]

ABSTRACT

We present evidence for widespread relativistic effects in the central regions of active galactic nuclei. In a sample of 18 Seyfert 1 galaxies observed by *ASCA*, 14 show an iron Kα line that is resolved, with mean width $\sigma_{K\alpha} = 0.43 \pm 0.12$ keV for a Gaussian profile (full width at half-maximum, FWHM $\sim 50,000$ km s^{-1}). However, many of the line profiles are asymmetric. A strong red wing is indicative of gravitational redshifts close to a central black hole, and accretion disk models provide an excellent description of the data.

The peak energy of the line is 6.4 keV, which indicates that it arises by fluorescence in near-neutral material. Our fits imply a low inclination for the disk in these Seyfert 1 galaxies, with a mean of 30°, consistent with orientation-dependent unification schemes. Differences in the line profiles from source to source imply slight variations in geometry, which cannot be accounted for solely by inclination. In most cases, we require that the line emission arises from a range of radii. Although a small contribution to the emission from a region other than the disk is not ruled out, it is not generally required and has little effect on our conclusions regarding the disk line. Our data are fit equally well with rotating (Kerr) and nonrotating (Schwarzschild) black hole models. We find a mean spectral index in the 3–10 keV range of $\langle \Gamma_{3-10} \rangle = 1.91 \pm 0.07$ after accounting for the effects of reflection.

Such observations probe the innermost regions of active galactic nuclei and arguably provide the best evidence yet obtained for the existence of supermassive black holes in the centers of active galaxies.

Subject headings: galaxies: active — galaxies: nuclei — galaxies: Seyfert — X-rays: galaxies

1. INTRODUCTION

The X-ray spectra of Seyfert 1 galaxies can contain numerous components. The continuum has an apparent power-law form, which covers several decades in energy. This is attenuated at soft X-ray energies by absorption both in the interstellar medium in our Galaxy and by material local to the active galaxy. An emission line from iron Kα has been observed at 6–7 keV in the vast majority of sources. A hard component affects the spectrum above ~ 10 keV, which is probably produced by Compton scattering ("reflection") of the continuum in the material that produces the line. In the soft X-ray regime, many sources have "soft excess" emission and can show emission features from oxygen and/or iron-L.

At least three nuclear emission/absorption regions are envisaged to account for these components. The region that emits the primary X-ray continuum may consist of hot and/or relativistic electrons and/or electron-positron pairs that Compton-upscatter softer "seed" photons. Compton-thick material in a low state of ionization, which may be identified with an accretion disk, gives rise to the iron Kα line, the reflection continuum and possibly the "soft excess." In many cases, the local absorption is due to a Compton-thin "warm absorber": highly ionized gas identified by features due to oxygen and iron, which may also produce the soft X-ray lines.

Detailed measurement of the various emission and absorption features and continua can therefore yield information regarding the physical conditions of the regions, such their dynamics, geometry, and ionization state. Of particular interest in this regard is the iron Kα emission line. These lines were first discovered with *HEAO 1* in heavily obscured Seyfert galaxies, such as NGC 4151 (Warwick et al. 1989 and references therein), and a number of narrow emission line galaxies (Mushotzky 1982). Not until the launch of *Ginga* was iron Kα emission recognized as an important, and possibly universal, property of Seyfert galaxies (Nandra & Pounds 1994, hereafter NP94, and references therein). From the time of their discovery in relatively unabsorbed active galactic nuclei (AGNs), the emission lines have been assigned an origin in material intimately associated with the accretion process, the most promising candidates being an accretion disk, or "blobs" of material surrounding the central source (Guilbert & Rees 1988; Fabian et al. 1989; Nandra et al. 1989; Pounds et al. 1990). However, for individual sources, the properties of the line were not generally well determined, given the limited spectral resolution of *Ginga*.

NP94 have discussed the properties of the iron Kα line in some detail, using a sample of Seyfert galaxies. The mean energy was found to be ~ 6.4 keV, which indicates that the most likely origin for the line is fluorescence in near-neutral material. Given this information, it can be deduced that the line cannot arise in material uniformly covering the source. The mean equivalent width of the line of 140 eV requires a high optical depth for the material, which would produce considerably more soft X-ray absorption in these objects than is observed. Indeed, the equivalent width of the line is sufficiently high to indicate that the material may be optically thick to Compton scattering. Further evidence for a Compton-thick region exists in the form of the "hard tail," which can be produced by "reflection" from the line-producing region. Given this evidence, an accretion disk is an obvious source for these features, especially when one

[1] Laboratory for High Energy Astrophysics, Code 660, NASA/Goddard Space Flight Center, Greenbelt, MD 20771.
[2] NAS/NRC Research Associate.
[3] Universities Space Research Association.

considers that the strengths of both the line and "reflection" component imply a covering fraction of $\sim 50\%$ for the material. Nonetheless, the "blob" geometry was not ruled out by the *Ginga* data (Bond & Matsuoka 1993; Nandra & George 1994).

Further impetus for the study of iron Kα lines in Seyfert galaxies has come from more recent *ASCA* data, which have indicated that this feature may be a key element in our understanding of AGNs. The earliest data showed good evidence that the emission lines were resolved (Fabian et al. 1994; Mushotzky et al. 1995), which confirms tentative suggestions from the *Ginga* data (NP94). Most dramatically, high signal-to-noise ratio data for two sources have shown characteristic line profiles (MCG -6-30-15, Tanaka et al. 1995; NGC 4151, Yaqoob et al. 1995). The lines in these sources are extremely broad, with FWHM implying relativistic velocities of order $0.2c$. Furthermore, there is a strong asymmetry to the red, which is indicative of the gravitational redshifts associated with the inner regions of an accretion disk surrounding the black hole. Fabian et al. (1995) concluded that this was the most plausible explanation for such profiles, rejecting other interpretations such as Comptonization. While it is tempting to extrapolate such a model and apply it to all AGNs, we must bear in mind that these extraordinary profiles are relatively rare in the literature. Further reinforcement of the black hole/accretion disk paradigm requires confirmation of that model for further sources. It is our intention to explore such avenues in the present paper.

In a previous paper (Nandra et al. 1997, hereafter Paper I), we have presented imaging and timing data for a sample of Seyfert 1 galaxies observed by *ASCA*. Here we present corresponding spectral data in the 3–10 keV regime in order to define the properties of the iron line. In § 2 we describe our analysis techniques. We will present the spectra in the full band in a subsequent paper (George et al. 1997, hereafter Paper III). Following that, § 3 presents

simple parameterizations for the iron Kα line. In § 4, we test specific disk-line models. Our aim thereby is to determine if such models, which have successfully described the two sources mentioned above, are generally applicable. In § 5, we compare our results to previous X-ray observations. We summarize our findings in § 6 and discuss them in § 7.

2. DATA ANALYSIS

In the present paper, we examine the spectra of a sample of Seyfert 1 galaxies observed by *ASCA* in the 3–10 keV band. We chose this energy range as it is relatively free from the effects of absorption, either by cold gas or the ionized "warm absorber," allowing us to attempt a definition of the continuum shape and, particularly, the iron Kα emission line. Furthermore, we consider only the time-averaged spectrum for each observation in order to maximize the signal-to-noise ratio. Our sample is listed in Table 1. We refer to each observation using the name of the source and, in cases where there are multiple observations, the observation number in parentheses [e.g., NGC 4151(2) is the second observation of NGC 4151; note that rejected observations are still assigned a number—see Paper I for details]. The selection criteria, observation log, and data analysis methods are presented in Paper I. Briefly, we have employed data from the US public archive at NASA/GSFC. We applied standard criteria for rejecting poor quality data and then extracted the source spectra using the FTOOLS/XSELECT package from both the Solid State Imaging Spectrometers (SISs) and Gas Imaging Spectrometers (GISs). Background spectra were extracted from source-free regions.

For both instruments we considered only the gain-corrected (Pulse-Invariant or PI) channels. The raw spectra were rebinned such that each resultant channel had at least 20 counts per bin, which permitted us to use χ^2 minimization for spectral fitting. All such fits were undertaken using the XSPEC package (v9.0). Calibration data were

TABLE 1
The *ASCA* Seyfert 1 Sample

Name	R.A. (1950)	Decl. (1950)	Redshift (V93)	N_H (Gal)[a] (10^{20} cm^{-2})	N_{obs}[b]/N_{tot}	log L_X[c] (ergs s^{-1})
Mrk 335	00 03 45.1	19 55 29	0.025	3.7	1/1	43.42
Fairall 9...............	01 21 51.0	-59 03 54	0.046	3.2	1/1	44.26
3C 120	04 30 31.5	05 14 59	0.033	12.3	1/1	44.34
NGC 3227	10 20 46.9	20 07 06	0.003	2.1	1/1	42.01
NGC 3516	11 03 22.8	72 50 18	0.009	2.9	1/1	43.43
NGC 3783	11 36 33.0	-37 27 42	0.009	9.6	2/2	43.25
NGC 4051	12 00 36.3	44 48 35	0.002	1.3	1/1	41.56
NGC 4151	12 08 00.9	39 40 59	0.003	2.2	3/6	42.97
Mrk 766	12 15 55.7	30 05 25	0.012	1.8	1/1	43.08
NGC 4593	12 37 04.6	-05 04 11	0.009	2.0	1/1	43.06
MCG -6-30-15......	13 33 01.4	-34 02 27	0.008	4.1	2/2	43.07
IC 4329A	13 46 28.2	-30 03 42	0.016	4.6	1/1	43.94
NGC 5548	14 15 43.6	25 21 58	0.017	1.6	1/1	43.76
Mrk 841	15 01 36.2	10 37 53	0.036	2.2	2/2	43.82
NGC 6814	19 39 55.7	-10 26 35	0.006	9.8	1/3	41.28
Mrk 509	20 41 26.1	-10 54 16	0.035	4.4	1/1	44.38
NGC 7469	23 00 44.4	08 36 17	0.017	4.8	1/3	43.60
MCG -2-58-22......	23 02 07.2	-08 57 20	0.047	3.5	1/1	44.14

NOTE.—Units of right ascension are hours, minutes, and seconds, and units of declination are degrees, arcminutes, and arcseconds. Redshifts are from V93, and N_H values are from Elvis, Lockman, & Wilkes 1989, Stark et al. 1992, Murphy et al. 1996, or Dickey & Lockman 1990.
[a] Galactic H I column density from 21 cm measurements.
[b] Number of observations for which adequate data were obtained/Total number of observations.
[c] Mean 2–10 keV luminosity.

TABLE 2

NARROW-LINE FITS

Name	A^a	Γ_{3-10}^b	$E_{K\alpha}^c$ (keV)	$I_{K\alpha}^d$	$W_{K\alpha}^e$ (eV)	χ_{NL}^2/d.o.f.	F_2^f
Mrk 335	0.29	1.87 ± 0.10	$6.37^{+0.16}_{-0.16}$	$1.2^{+0.7}_{-0.8}$	110^{+60}_{-70}	227.9/252	5.0
Fairall 9	0.60	1.83 ± 0.06	$6.33^{+0.15}_{-0.08}$	$2.9^{+0.9}_{-1.0}$	120^{+40}_{-40}	640.6/610	15.0
3C 120	1.31	1.79 ± 0.03	$6.37^{+0.05}_{-0.05}$	$3.5^{+0.6}_{-1.7}$	70^{+10}_{-30}	881.9/950	15.9
NGC 3227...............	0.48	1.52 ± 0.04	$6.42^{+0.04}_{-0.04}$	$3.5^{+0.9}_{-0.9}$	120^{+30}_{-30}	885.3/920	30.2
NGC 3516...............	2.03	1.74 ± 0.03	$6.37^{+0.03}_{-0.03}$	$7.9^{+2.1}_{-1.3}$	90^{+20}_{-10}	1055.3/1004	42.8
NGC 3783(1)	1.03	1.57 ± 0.05	$6.38^{+0.04}_{-0.04}$	$8.3^{+1.8}_{-1.8}$	150^{+30}_{-30}	800.8/788	34.2
NGC 3783(2)	1.11	1.51 ± 0.05	$6.16^{+0.14}_{-0.06}$	$5.7^{+2.1}_{-2.1}$	80^{+30}_{-30}	715.1/743	27.4
NGC 4051...............	0.73	1.92 ± 0.06	$6.44^{+0.07}_{-0.07}$	$2.8^{+0.7}_{-1.2}$	140^{+35}_{-60}	672.4/657	13.3
NGC 4151(2)	3.75	1.42 ± 0.12	$6.40^{+0.02}_{-0.03}$	29^{+5}_{-7}	110^{+20}_{-30}	760.4/693	63.2
NGC 4151(4)	6.31	1.59 ± 0.07	$6.36^{+0.05}_{-0.05}$	32^{+9}_{-6}	90^{+30}_{-20}	1409.1/1401	47.2
NGC 4151(5)	7.73	1.65 ± 0.05	$6.37^{+0.02}_{-0.02}$	31^{+6}_{-5}	90^{+20}_{-20}	1348.6/1228	45.0
Mrk 766	0.75	2.00 ± 0.05	$6.37^{+0.03}_{-0.03}$	$2.6^{+1.0}_{-0.7}$	140^{+50}_{-40}	584.3/682	21.2
NGC 4593...............	0.92	1.78 ± 0.05	$6.35^{+0.05}_{-0.05}$	$3.1^{+1.3}_{-1.1}$	90^{+40}_{-30}	827.4/868	12.7
MCG -6-30-15(1)......	1.64	1.94 ± 0.05	$6.26^{+0.07}_{-0.10}$	$3.2^{+1.4}_{-1.3}$	70^{+30}_{-30}	943.4/845	9.0
MCG -6-30-15(2)......	1.11	1.81 ± 0.05	$6.38^{+0.07}_{-0.10}$	$3.8^{+0.9}_{-2.0}$	100^{+20}_{-50}	829.7/802	9.7
IC 4329A	1.95	1.70 ± 0.03	$6.32^{+0.05}_{-0.05}$	$7.3^{+1.4}_{-1.6}$	80^{+20}_{-20}	1297.7/1249	38.5
NGC 5548...............	1.24	1.75 ± 0.04	$6.39^{+0.04}_{-0.04}$	$4.6^{+1.3}_{-1.3}$	90^{+30}_{-30}	973.6/1000	21.6
Mrk 841(1)	0.38	1.84 ± 0.09	$6.37^{+0.12}_{-0.02}$	$2.4^{+0.9}_{-0.8}$	170^{+60}_{-60}	378.1/368	7.0
Mrk 841(2)	0.21	1.57 ± 0.10	$6.53^{+0.07}_{-0.16}$	$1.4^{+1.0}_{-0.9}$	120^{+90}_{-80}	181.9/203	4.7
NGC 6814(1)	0.02	1.54 ± 0.26	$5.9^{+0.6}_{-0.2}$	$0.4^{+0.3}_{-0.3}$	230^{+170}_{-170}	68.1/76	4.1
Mrk 509	1.21	1.76 ± 0.05	$6.37^{+0.07}_{-0.07}$	$3.5^{+0.7}_{-2.4}$	70^{+10}_{-50}	819.0/896	7.4
NGC 7469(2)	0.76	1.78 ± 0.07	$6.39^{+0.06}_{-0.05}$	$3.8^{+1.6}_{-1.5}$	130^{+50}_{-50}	501.1/451	19.7
MCG -2-58-22	0.29	1.58 ± 0.08	$6.33^{+0.18}_{-0.07}$	$2.6^{+0.8}_{-1.8}$	150^{+100}_{-50}	408.4/388	7.8

NOTE.—Fits were undertaken in the 3–10 keV range. Absorption is by Galactic N_H only, except in the case of NGC 4151, where the column was left free. Error bars on the fit parameters are 68% confidence limits for three interesting parameters ($\Delta\chi^2 = 3.5$).

[a] Power-law flux at 1 keV; 10^{-3} photons cm^{-2} s^{-1} keV^{-1}.
[b] Power-law index.
[c] Energy of the emission line in the rest frame of the source.
[d] Flux of the line; 10^{-5} photons cm^{-2} s^{-1}.
[e] Line equivalent width.
[f] F-statistic for the addition of two free parameters.

taken from the HEASARC calibration database. The SIS response matrices were released on 1994 November 9 and the GIS matrices on 1995 March 6. Effective areas were calculated using the standard software, which does not include a parameterization of the azimuthal dependence of the point-spread function. This can cause inaccuracies in the normalization, particularly in the case in which the source region is not circular. Uncertainties in determining the source centroid can also result in normalization errors, and the cross-calibration of the four instruments is not known to arbitrarily high accuracy. These factors lead to cross-calibration uncertainties among the four instruments, but as the response of the XRT is not strongly dependent on energy, we do not expect them to introduce distortions into the individual spectra. We therefore chose to fit all four *ASCA* detectors simultaneously with the same model but allowed the normalization of that model to be free for each detector.

Owing to radiation damage, the response of the CCD detectors is changing slowly with time (Dotani et al. 1995). The main effects of this damage relevant to the analysis presented here are small changes in the energy scale and a degradation of the energy resolution. We have not accounted for such effects, which are most pronounced in 4-CCD mode data. However, even in this most extreme case, we expect the effects to be small for our data, which

were taken early in the mission. The estimated offset and resolution changes are < 50 eV for 4-CCD mode and are negligible for 1- and 2-CCD modes for data taken < 1 yr after launch (Dotani et al. 1995). Normalizations and fluxes quoted for the sources will be for the SIS0 detector. Typically, the two SIS detectors agree in flux to within $\sim 1\%$–3% but are higher than the GIS by $\sim 10\%$–20%.

2.1. Statistical Considerations

As mentioned above, we have employed χ^2 minimization for spectral fitting (Lampton, Margon, & Bowyer 1976). Although this forces us to rebin the data arbitrarily, sometimes beyond the spectral resolution of the instrument, we prefer this over maximum likelihood methods such as the *C*-statistic (Cash 1979) because the data can be background subtracted. This is highly desirable in cases, such as these, where reliable background models have not yet been developed. Although the background represents typically only a few percent of the total count rate in the 3–10 keV band, it can have a significant effect at high energies. We therefore note here the fact that we have not accounted for vignetting of the diffuse X-ray background when calculating our background rates nor any other variations in the background rates over the detectors. Such effects are not currently well understood for *ASCA* data. Our chosen bin size is not optimal for determining the goodness of fit; at low energies,

the data are underbinned compared to the resolution of the detector. We prefer this to the alternative of overbinning, which would sacrifice spectral information essential to our determination of the line parameters. Although detailed justification for our choice of 20 counts per bin requires simulations beyond the scope of this paper, a comparison of our spectra with the simulations of Nousek (1990) suggests that using a Gaussian approximation and χ^2 minimization will introduce uncertainties of the order of 1% to our derived parameters, smaller than the typical statistical error.

Once the minimum χ^2 value is found in each fit, confidence regions for the parameters have been determined using the prescription of Lampton et al. (1976). Unless otherwise stated, we have calculated the confidence region by projection of the joint confidence region defined by the number of "interesting" parameters, as recommended by Lampton et al. We have considered the model normalizations as uninteresting. This is because we do not expect the origin of the difference in the normalizations— uncertainties in the effective areas—to affect the spectral form. Thus the number of interesting parameters that we have used to calculate the χ^2 deviates is given by $N_{\rm fr} - 4$, where $N_{\rm fr}$ is the number of free parameters in the model. Specific $\Delta\chi^2$ values are shown as footnotes to the tables. For completeness, we have quoted the best-fit normalization for one of the models in Table 2, although we have not attempted to determine the confidence interval for that parameter, as we consider it uninteresting.

In most cases we quote the 68% confidence limits for the parameters, which is the same confidence level as the 1 σ distribution of a Gaussian. Furthermore, in some specific circumstances, we have gone on to interpret the 68% confidence limit as if it were the 1 σ error bar of a Gaussian distribution. Examples are the calculation of the weighted mean and the determination of the mean and dispersion using the maximum-likelihood method. This assumes that the confidence surface is itself Gaussian, which is often a poor approximation. However, this is unimportant, as long as the Gaussian approximation does not underestimate the true confidence region. We believe this to be true in most circumstances. However, in most cases the confidence region is asymmetric, which results in two-sided "error bars." In all such cases, we use the larger uncertainty as our 1 σ error bar. Furthermore, where the 68% confidence region overlaps the limits of the allowed parameter values (e.g., where the inclination reaches 0° or 90°), we assume that the 1 σ error bar is essentially infinite, thus placing no weight on the derived value. This is a highly conservative approach that should avoid any spurious results arising from our use of confidence regions as Gaussian error bars.

In comparing various models for the X-ray spectra, and particularly the iron lines, we have employed various statistical tests, including the acceptability of χ^2, although as noted above, our data are not optimally binned to maximize χ^2; the F-test (see, e.g., Bevington 1969), which has been employed to determine whether additional components, or parameters, provide a significant improvement; the likelihood ratio (Edwards 1972; Mushotzky 1982), which has been used to determine whether models with the same number of free parameters are more or less likely to produce the observed data. We have adopted the 95% confidence level in assessing whether or not various features are real, but we bear in mind that for a sample of 23 (or more often 22) observations, this will typically result in one spurious detection each time the sample is considered as a whole.

3. IRON Kα EMISSION: SIMPLE PARAMETERIZATIONS

We first attempted some simple spectral fits to the *ASCA* data, without reference to a specific, physical model.

3.1. *Narrow Lines*

Our initial fit was of a power law with a Gaussian component with width, $\sigma = 10$ eV, to represent the iron line. This width is smaller than the instrumental response and therefore is effectively "narrow" for our purposes. In practice, this fit will model any line emission up to the width of the spectral response of ~ 120 eV (FWHM) at 6 keV. The Gaussian provides a significant improvement in the fit in all 18 sources, which confirms that iron Kα emission is extremely common in Seyfert 1 galaxies. The details of these narrow-line fits are shown in Table 2. The energies quoted are in the rest frame throughout. Three of the fits are unacceptable at $>95\%$ confidence: NGC 4151(2), NGC 4151(5), and MCG -6-30-15(1). The mean values of the parameters derived from these fits are shown in Table 9. That table shows the unweighted mean and standard deviation (col. [3]), the weighted mean and uncertainty (col. [4]), and in columns (5) and (6), estimates of the mean and dispersion of the parent population, calculated using the maximum likelihood method of Maccacaro et al. (1988). We consider the latter two values to be most appropriate for determining the average properties of the sample, and quote these in the text. A histogram of the line energies and equivalent widths is shown in the upper panels of Figure 1. Confirming and extending the *Ginga* results, our *ASCA* observations show a strong preference for iron in a relatively low state of ionization, with the mean energy of $\langle E_{\rm K\alpha} \rangle = 6.36 \pm 0.02$ keV, which is even indicative of a small net redshift (but only at $\sim 90\%$ confidence). There is no measured dispersion in these values, with an upper limit of 60 eV; the large deviation in the case of NGC 6814 is due its large measurement error, as it is a factor >10 weaker than all other sources. The lack of dispersion is remarkable; any systematic deviations in the energy scale due to residual calibration errors (see § 2) must be smaller than this. Also note that the differences in the *observed-frame* energy between the sources is ~ 300 eV. We find a mean ionization state $<$Fe XVI ($E_{\rm K\alpha} < 6.41$) at the 99% confidence level. The mean equivalent width of 98 ± 12 eV for these narrow lines is only $\sim 70\%$ of the corresponding value derived by *Ginga* (140 eV; NP94). An examination of the residuals makes clear why this is the case. In a number of sources the line flux clearly extends beyond the bounds of the spectral response function, indicating the line has a significant width. The wider response of *Ginga* would result in more of this flux being modeled in a fit that is effectively a delta-function profile. Such a profile is clearly not appropriate for our higher resolution *ASCA* data, and we now go on to describe this more quantitatively.

3.2. *Broad Lines*

Some *Ginga* spectra of Seyfert galaxies showed a significant improvement in the fit when the line width was allowed to be a free parameter (NP94). Owing to the nature of the *Ginga* spectral response, this implied huge line widths of
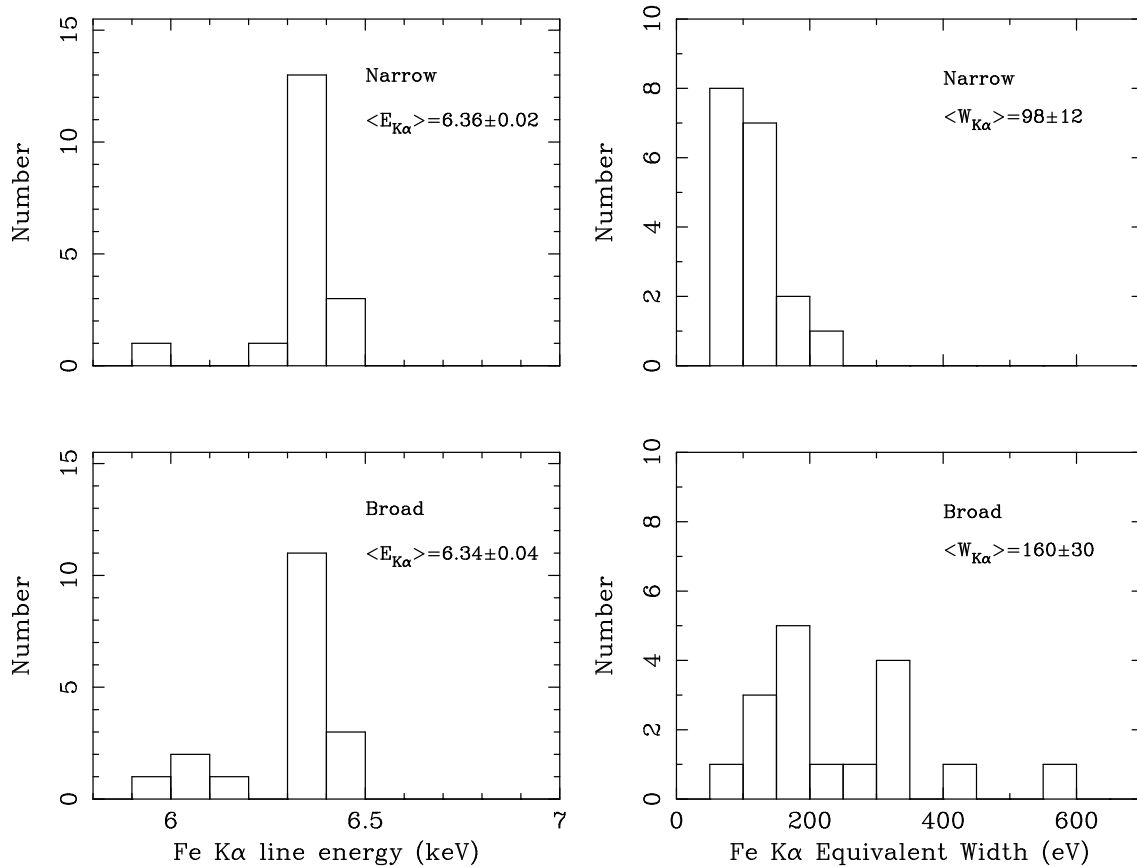
Fig. 1.—Histograms of the line energy (*left-hand panels*) and the equivalent width (*right-hand panels*) for the sources in our sample. Where multiple observations exist, the weighted mean value has been adopted. The upper panels show the values obtained when the line is assumed to be narrow relative to the instrumental response (Table 2), whereas the lower plots show the values when the line width is left as a free parameter (Table 3). In both cases, the mean line energy is found to be very close to the 6.4 keV expected of neutral iron, even being consistent with a mild redshift. The equivalent widths in the broad-line fits are typically $\sim 50\%$ larger than for a narrow line.

order 1 keV in the cases in which significant broadening was indicated. This led NP94 to speculate that the apparent broadening might be spurious, instead reflecting unmodeled continuum components. Improved spectral resolution is the key to removing this ambiguity. Indeed, early *ASCA* observations showed that, at least in some cases, the iron line was significantly broadened (see, e.g., Mushotzky et al. 1995). We tested this for our sources by allowing the width of the Gaussian, σ, to be a free parameter. The results of these fits are shown in Table 3. A total of 18/23 observations and 14/18 sources showed a significant improvement, with only two fits just unacceptable at the 95% confidence level: NGC 4151(2) and MCG -6-30-15(1). In cases in which the line width is not detected, we have shown only the 90% upper limit to the line width. These are all consistent with the mean value of $\langle \sigma_{K\alpha} \rangle = 0.43 \pm 0.12$ keV (Table 9). This corresponds to a FWHM of approximately 47,000 km s^{-1}. A histogram of the line widths is shown in Figure 2.

Once again, the energy of these broad lines strongly indicates that material in a low ionization state is the source of the line, with a mean energy $\langle E_{K\alpha} \rangle = 6.34 \pm 0.04$ keV. The 99% confidence upper limit to the energy of 6.41 keV again corresponds to an ionization state for iron $<$ Fe XVI—above this ionization state the line rises sharply in energy (Makishima 1985). If the material were in collisional ionization equilibrium, this corresponds to a temperature of $\lesssim 3 \times 10^6$ K (Arnaud & Raymond 1992). Of course, any material close to the central source is more likely to be
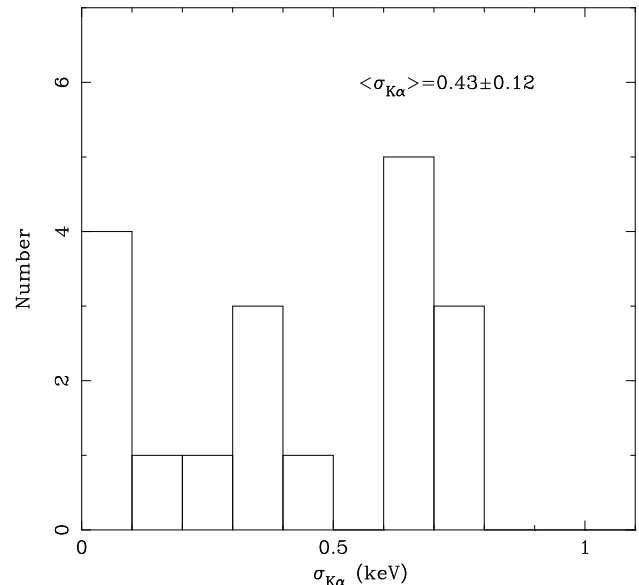

Fig. 2.—Histogram of the line widths obtained from the broad Gaussian fit. In the cases where no significant improvement is obtained when $\sigma_{K\alpha}$ is a free parameter, the point has been added to the lowest bin. In 14 of the 18 sources the line is resolved, with $\langle \sigma_{K\alpha} \rangle = 0.43 \pm 0.12$, which corresponds to a FWHM $\sim 50,000$ km s^{-1}. This implies highly relativistic motions if the width is due to velocity broadening.

TABLE 3

BROAD-LINE FITS

Name	Γ_{3-10}	$E_{K\alpha}$	$W_{K\alpha}$	$\sigma_{K\alpha}$[a]	F_1[b]
Mrk 335	...	...	...	<1.1	0.9
Fairall 9	$1.91^{+0.08}_{-0.08}$	$6.36^{+0.14}_{-0.14}$	320^{+130}_{-80}	$0.35^{+0.18}_{-0.11}$	21.7
3C 120	$1.89^{+0.08}_{-0.06}$	$6.39^{+0.20}_{-0.20}$	330^{+200}_{-130}	$0.74^{+0.34}_{-0.27}$	39.9
NGC 3227	$1.52^{+0.08}_{-0.03}$	$6.30^{+0.12}_{-0.12}$	180^{+60}_{-50}	$0.25^{+0.12}_{-0.10}$	7.6
NGC 3516	$1.83^{+0.05}_{-0.05}$	$6.12^{+0.13}_{-0.15}$	340^{+130}_{-110}	$0.64^{+0.22}_{-0.19}$	40.1
NGC 3783(1)	$1.70^{+0.11}_{-0.08}$	$6.11^{+0.17}_{-0.18}$	510^{+490}_{-190}	$0.71^{+0.35}_{-0.28}$	19.3
NGC 3783(2)	$1.60^{+0.04}_{-0.08}$	$5.93^{+0.26}_{-0.39}$	360^{+300}_{-180}	$0.70^{+0.48}_{-0.36}$	24.3
NGC 4051	...	...	...	<1.4	1.8
NGC 4151(2)	$1.44^{+0.14}_{-0.13}$	$6.39^{+0.05}_{-0.05}$	130^{+60}_{-40}	$0.10^{+0.08}_{-0.10}$	4.3
NGC 4151(4)	$1.57^{+0.10}_{-0.11}$	$6.14^{+0.13}_{-0.18}$	340^{+160}_{-110}	$0.56^{+0.25}_{-0.19}$	52.6
NGC 4151(5)	$1.58^{+0.09}_{-0.11}$	$5.92^{+0.12}_{-0.17}$	330^{+140}_{-90}	$0.64^{+0.22}_{-0.15}$	50.1
Mrk 766	$2.16^{+0.15}_{-0.11}$	$6.03^{+0.24}_{-0.25}$	550^{+390}_{-230}	$0.72^{+0.36}_{-0.25}$	16.0
NGC 4593	...	...	...	<1.1	3.4
MCG -6-30-15(1)......	$2.04^{+0.10}_{-0.07}$	$6.06^{+0.22}_{-0.21}$	320^{+110}_{-90}	$0.62^{+0.24}_{-0.18}$	27.3
MCG -6-30-15(2)......	$1.95^{+0.12}_{-0.08}$	$5.80^{+0.25}_{-0.27}$	460^{+280}_{-140}	$0.88^{+0.43}_{-0.23}$	32.1
IC 4329A	$1.71^{+0.03}_{-0.03}$	$6.34^{+0.07}_{-0.05}$	110^{+40}_{-30}	$0.14^{+0.12}_{-0.08}$	10.7
NGC 5548	$1.79^{+0.05}_{-0.05}$	$6.41^{+0.16}_{-0.14}$	170^{+60}_{-40}	$0.34^{+0.19}_{-0.12}$	5.8
Mrk 841(1)	$2.00^{+0.20}_{-0.15}$	$6.15^{+0.25}_{-0.28}$	580^{+400}_{-290}	$0.63^{+0.35}_{-0.32}$	6.9
Mrk 841(2)	...	...	...	$<\infty$	0.9
NGC 6814(1)	$1.9^{+2.0}_{-0.5}$	$6.3^{+0.7}_{-0.4}$	1100^{+2100}_{-800}	$0.6^{+0.8}_{-0.4}$	8.9
Mrk 509	$1.82^{+0.09}_{-0.07}$	$6.35^{+0.25}_{-1.02}$	210^{+190}_{-130}	$0.47^{+0.50}_{-0.30}$	14.2
NGC 7469(2)	$1.84^{+0.12}_{-0.10}$	$6.39^{+0.24}_{-0.21}$	280^{+190}_{-170}	$0.37^{+0.31}_{-0.37}$	3.7
MCG -2-58-22	...	...	...	<0.85	1.7

NOTE.—Fits with a power-law plus broad-line to the *ASCA* data in the 3–10 keV range. Absorption is by Galactic N_H only, except in the case of NGC 4151, where the column was left free. Error bars on the fit parameters are 68% confidence limits for 4 interesting parameters ($\Delta\chi^2 = 4.7$).

[a] Width of the Gaussian (keV).

[b] F-statistic for the addition of σ as a free parameter.

photoionized than collisionally ionized, in which case the temperature is probably much lower.

The mean equivalent width of these broad lines is $\langle W_{K\alpha}\rangle = 160 \pm 30$ eV. This value is consistent with the mean determined by *Ginga* for a line of $\sigma = 0.1$ keV of 140 ± 20 eV. As mentioned above, a fit with a line that is narrow compared to the instrumental response of a given instrument will tend to model any line flux that has a width up to the spectral resolution. For the case of *Ginga*, this is equivalent to $\sigma \sim 0.5$ keV (Turner et al. 1989). This corresponds roughly to the mean width of the lines determined in our broad Gaussian fits. In this respect, then, the equivalent widths determined by *ASCA* and *Ginga* show a remarkable consistency.

3.3. *Line Profiles*

At least in some sources, the iron Kα line is not well modeled by a symmetrical profile such as a Gaussian. We have attempted to determine the line profiles in a relatively model-independent way, with the results shown in Figure 3. These were determined with a fit to the 3–10 keV SIS data only with a power law but excluding the iron band between 5 and 7 keV. We then multiplied the resultant data/model ratio by the best-fit continuum model. This results in an estimate of the line profile as seen in the observed frame, deconvolved from the instrumental response. Almost all of the sources show a clear excess, with broadening far greater than the instrumental response. It is also evident that a number of sources show skewed, asymmetric profiles. This could represent multiple line components (for instance,

there may be both broad and narrow components). However, many sources show the characteristic black hole/ accretion disk profile (Fabian et al. 1989; Laor 1991; Matt et al. 1992), in which case they may be predominantly one component.

To demonstrate this further, we have created a composite line profile for all 18 sources. This was achieved by transforming the above-mentioned data/model ratios into the rest frame of each source and taking the mean ratio in bins of width 40 eV. To estimate the mean line profile from these plots, we have multiplied by a continuum model defined by the mean values for the sample. This is shown in Figure 4a. In Figure 4b. we show the same plot excluding MCG -6-30-15 and NGC 4151 in order to investigate whether these sources dominate the mean profile. Several things are apparent from Figure 4:

The line profiles are clearly consistent, showing that our results are not biased by the inclusion of MCG -6-30-15 and NGC 4151.

The profiles are extremely broad ~ 2 keV full width at zero intensity (FWZI), which corresponds to velocities of order $0.3c$.

As in many of the individual sources, the profile consists of a relatively narrow core, with an underlying broad component.

The core peaks at an energy remarkably close to 6.4 keV.

The broadening is primarily to the red, with relatively little flux blueward of 6.4 keV and specifically no strong component due to helium-like or hydrogen-like iron (6.7–6.9 keV).
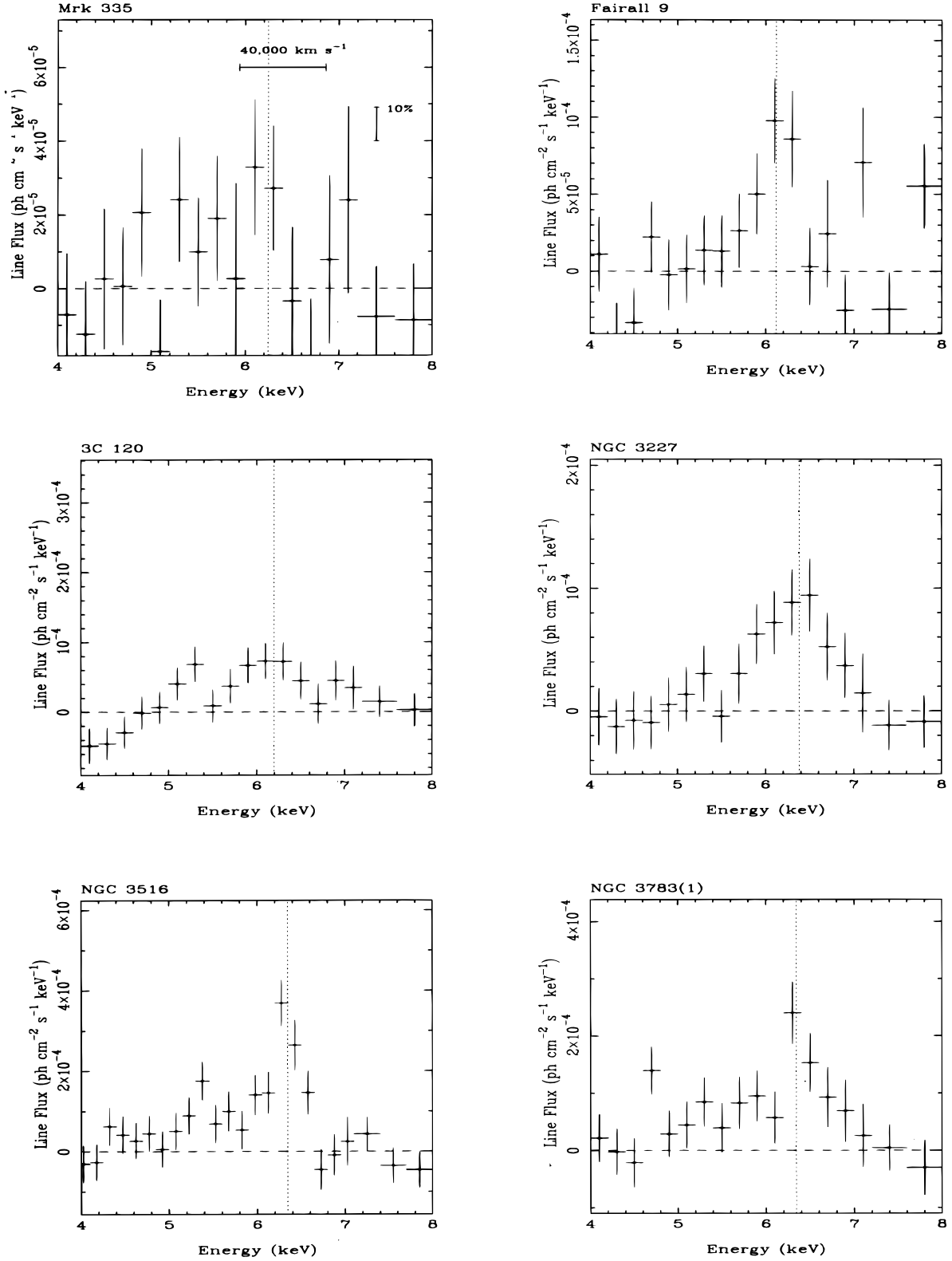
FIG. 3.—Profiles of the Fe Kα emission lines in our sample sources, measured by the SIS only. The continuum has been estimated by fitting a power law (with Galactic absorption) to the 3–5 and 7–10 keV SIS data and rebinning the resultant residuals. Most show significant broadening beyond the instrumental resolution, and some have the characteristic profile expected if the line is produced close to a central black hole: an asymmetry skewed to the red. All plots have been rescaled to a fixed fraction of the continuum at 6.4 keV. That energy (in the rest frame) is marked by a vertical dotted line in each plot. The first plot (Mrk 335) shows a horizontal scale in velocity space (corresponding to 40,000 km s^{-1} and a vertical bar that indicates a 10% variation from the continuum.

NGC 3783(2)

NGC 4051

NGC 4151(2)

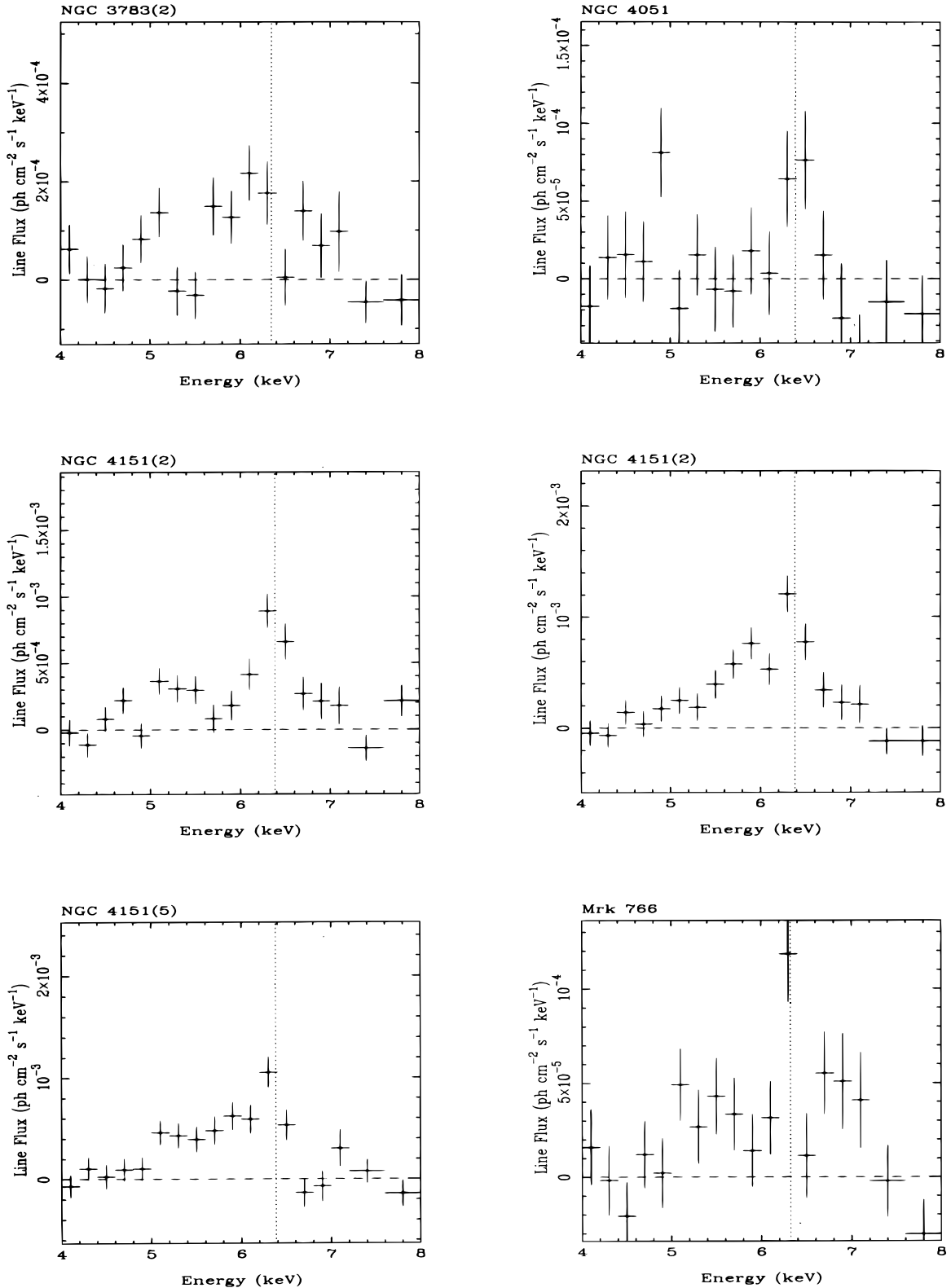NGC 4151(2)

NGC 4151(5)

Mrk 766

FIG. 3—*Continued*

To illustrate these more quantitatively, we have modeled the profiles with two Gaussians, following Tanaka et al. (1995). The resulting fit is shown in Figure 4a. The centroid energies of the core are 6.38 keV in both cases, with a width of $\sigma = 0.1$ keV. The broad component is strongly redshifted with centroid energy ~ 6 keV and width of $\sigma = 0.7$ keV and carries $\sim 75\%$ of the total flux. The dotted line in Figure 4b

shows the instrumental response. While some artificial broadening could result from radiation damage to the CCDs, particularly in 4-CCD mode, these residual calibration uncertainties of $\sim$few percent in this regime are much smaller than the observed deviations ($\sim 10\%$–20% in the red wing). To demonstrate this, we show in Figure 5 the residuals for our Seyfert sample compared to those for the

NGC 4593

MCG−6−30−15

MCG−6−30−15

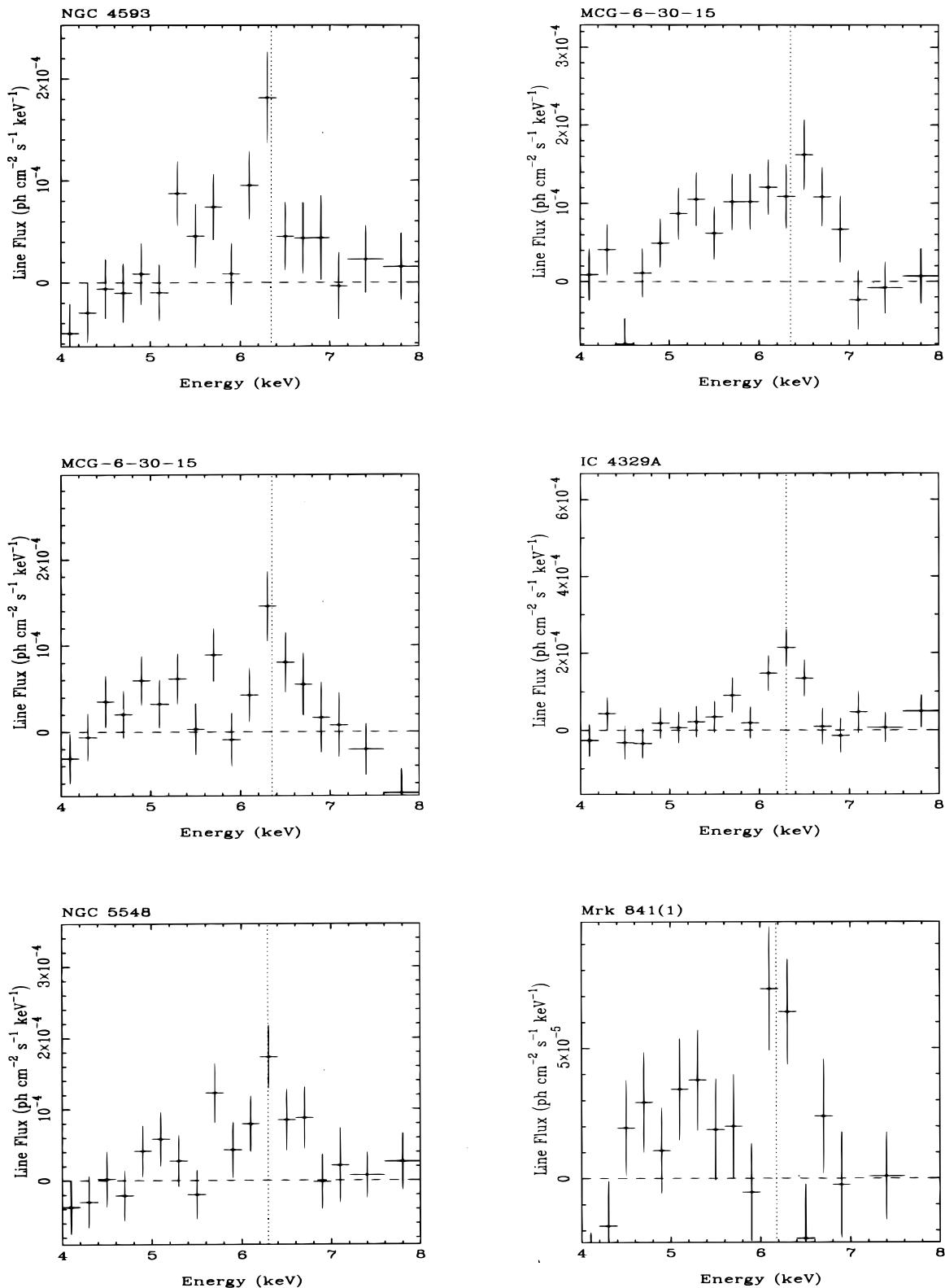IC 4329A

NGC 5548

Mrk 841(1)

FIG. 3—*Continued*

Coma Cluster and also the Dark Earth (essentially the particle background of the SIS; Gendreau 1995). All three plots show an emission line, but only the Seyfert galaxies show the red wing, which indicates that this feature is not due to a persistent calibration error.

It is also highly unlikely that emission lines from any other element contribute significantly to the emission in the 5–7 keV band. The other elements with K-shell energies (V, Cr, Mn, and Co) in this range have abundances and fluorescence yields which would lead to line intensities of a factor > 100 less than iron, to which we attribute the entire line flux. Iron line blends alone cannot account for the observed widths in most cases, as the line flux extends up to ~1.5 keV below the energy expected from neutral iron. Compton
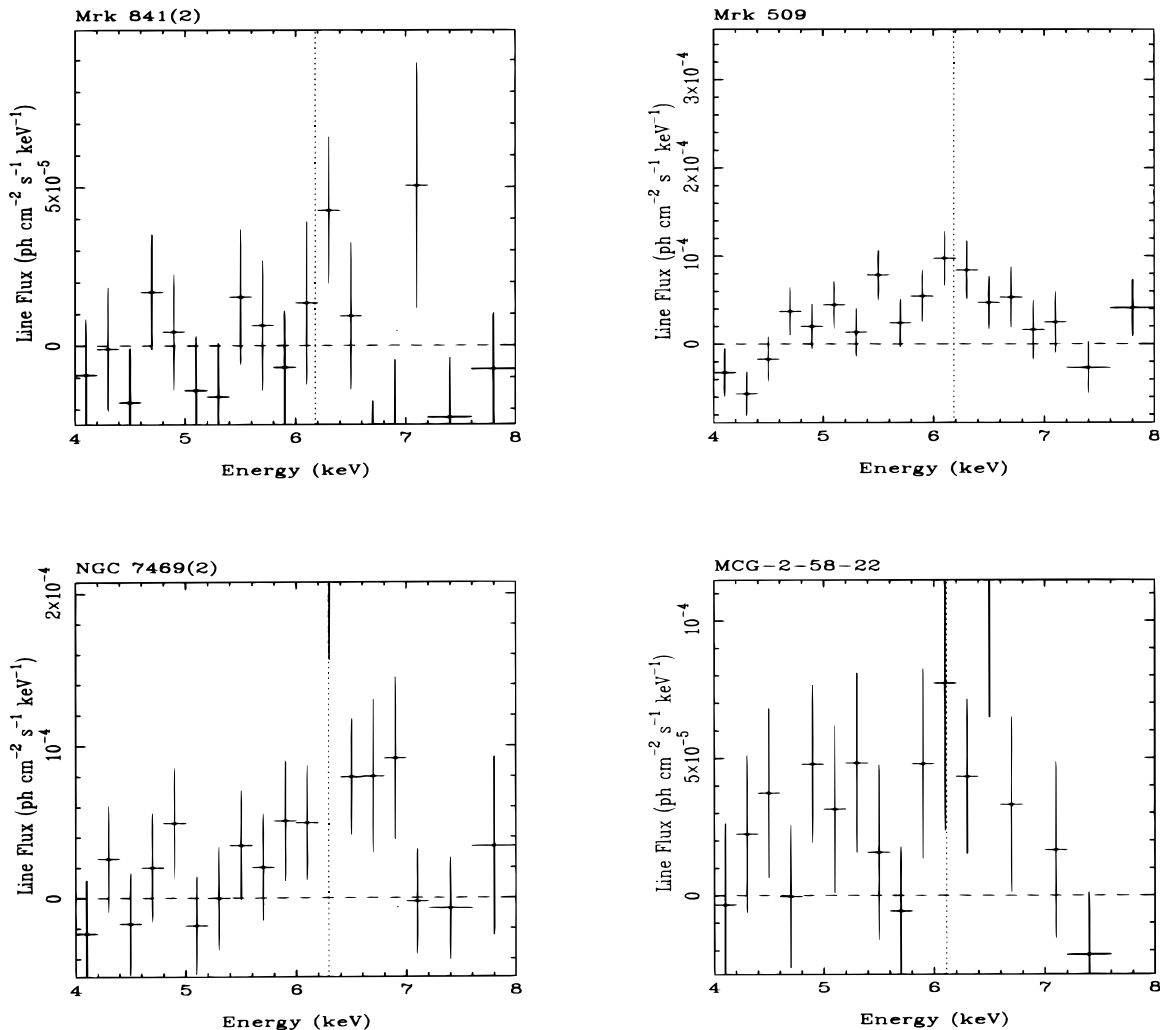
Fig. 3—*Continued*

downscattering can, in principle, redshift the line sufficiently, but many workers have argued against this mechanism (Mushotzky et al. 1995; Tanaka et al. 1995; Fabian et al. 1995). The dramatic redshifts and broadening expected due to special and general relativistic effects close to a black hole provide a plausible explanation for the observed line profiles. One class of models that has been successfully applied to *ASCA* observations of MCG −6-30-15 and NGC 4151 is that of an accretion disk (Tanaka et al. 1995; Yaqoob et al. 1995). The other sources apparently exhibit rather similar profiles and we now consider such models.

4. ACCRETION DISK MODELING

We will refer to a number of parameters in the following sections which characterize the disk-line models: the inner radius of the disk, R_i; the outer radius, R_o; the inclination of the axis of rotation with respect to the line of sight, i; the rest energy, $E_{K\alpha}$; and the line normalization, $I_{K\alpha}$. We excluded NGC 6814 from the following analysis as the signal-to-noise ratio is so much lower than that of the other sources, leaving 22 observations of 17 sources.

4.1. *Schwarzschild Model*

Our first test of the black hole/accretion disk hypothesis was using the model of Fabian et al. (1989). Their disk-line

model assumes a Schwarzschild geometry and computes the line profile only and not the strength. No specific geometry for the X-ray source is assumed, and therefore the line emissivity is parameterized by a power law as a function of radius, R^{-q}. The value of q can be a free parameter. For a pointlike X-ray source located above the center of the disk, we expect $q \sim 0$ in the inner regions, steepening to $q \sim 3$ at large radii. However, different emissivity profiles may be relevant, for example if there are multiple X-ray sources, or if the source is not pointlike compared to the line-emitting region.

The line profile has a strong dependence on q, as for values >2, the emission is concentrated in the inner disk, where extreme gravitational and Doppler effects operate. In these circumstances, R_o can rarely be constrained. Conversely, if the outer disk is the dominant source of line emission, poor or no constraints can be placed on R_i. We have therefore chosen to fix the inner and outer radii of the disk at $6R_g$ and $1000R_g$, respectively (where R_g is the gravitational radius of the black hole) and have used q as a parameterization not only of the geometry of the X-ray source but of the accretion disk itself. We allow the inclination of the disk to be a free parameter and also the normalization of the line. We will compare the strength of the lines to the disk model later. Finally, we assume $E_{K\alpha} = 6.4$ keV in the rest frame. As we showed in Tables 2 and 3 and Figures
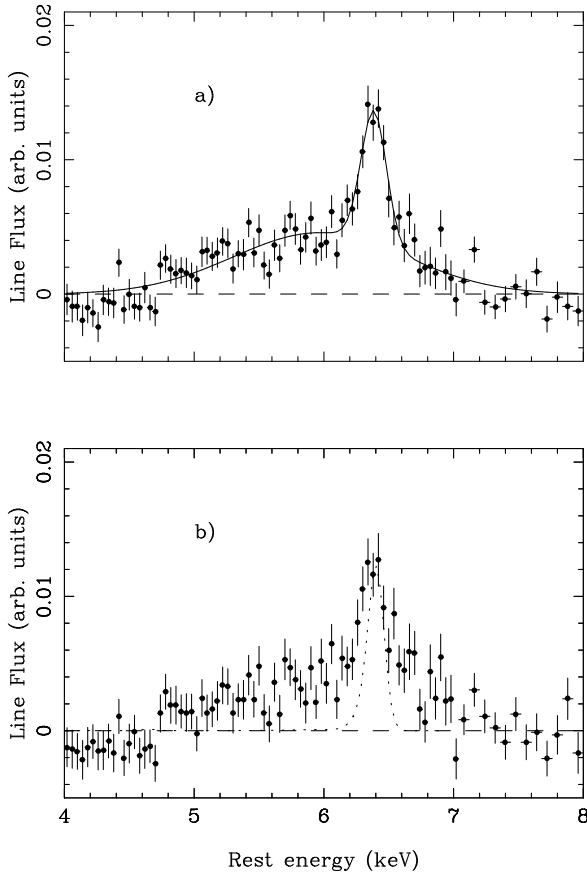
FIG. 4.—Mean line profiles for the sample. These were produced by transforming the data/model ratio for each source into the rest frame, rebinning the resultant residuals, and converting to flux space assuming the mean of the best-fit continua. Fig. 4a shows the results for the whole sample, while Fig. 4b shows the profile with the two previously reported skewed lines, MCG −6-30-15 and NGC 4151, removed. The two plots are clearly remarkably similar. The solid line in (a) is a double-Gaussian fit to the profile. The narrower component peaks at 6.4 keV with a width of $\sigma \sim 0.1$ keV. The broader component is strongly redshifted, with a centroid energy of 6.1 keV and a width of 0.7 keV. It also carries the bulk ($\sim 75\%$) of the flux. The dotted line in (b) is the spectral response of the ASCA SIS detectors at 6.4 keV.

FIG. 5.—Data/model residuals for our ASCA Seyfert 1 sample (top panel, used to create Fig. 4a); the Coma Cluster (middle panel). The continuum here has been fitted with a bremsstrahlung model, excluding the 5–7 keV region; and the Dark Earth. Here the continuum has been modeled with a power law excluding regions contaminated by lines, the most prominent of which are iron Kα and nickel Kα. Although all three panels show very clear evidence for emission lines, only the Seyfert 1 ensemble shows a red wing.

3 and 4, both the peak and mean line energies lie close to this value in all cases, with no evidence for a helium-like or hydrogen-like line.

The results of these disk-line fits are shown in Table 4 and depicted in Figure 6. There is a substantial improvement in the fit compared to the broad Gaussian model in a large number of cases, owing to the asymmetry of the profiles. All of the disk-line fits are acceptable at < 95% confidence. The total χ^2 for all 22 observations was 16,762.4 for the broad-line fit and 16,627.3 for the disk lines ($\Delta\chi^2 = 135.1$), which is highly significant as measured by the likelihood ratio (see § 2), which is shown in Table 8. The mean power-law index is similar to the broad-line fits $\langle\Gamma_{3-10}\rangle = 1.78 \pm 0.07$. However, the line equivalent width is rather larger, at $\langle W_{K\alpha}\rangle = 290 \pm 50$ eV. Typically, a low inclination ($\sim$face-on) disk is preferred in our fits. The mean inclination angle is $\langle i \rangle = 29° \pm 3°$. If the accretion disk were oriented randomly, we might expect a mean inclination of $\sim 60°$, which is not preferred in our fits. We comment on this later. The mean value of q, which parameterizes the geometry of the system is $\langle q \rangle = 2.5 \pm 0.4$. This is in good agreement with the value expected for a pointlike X-ray source above a flat
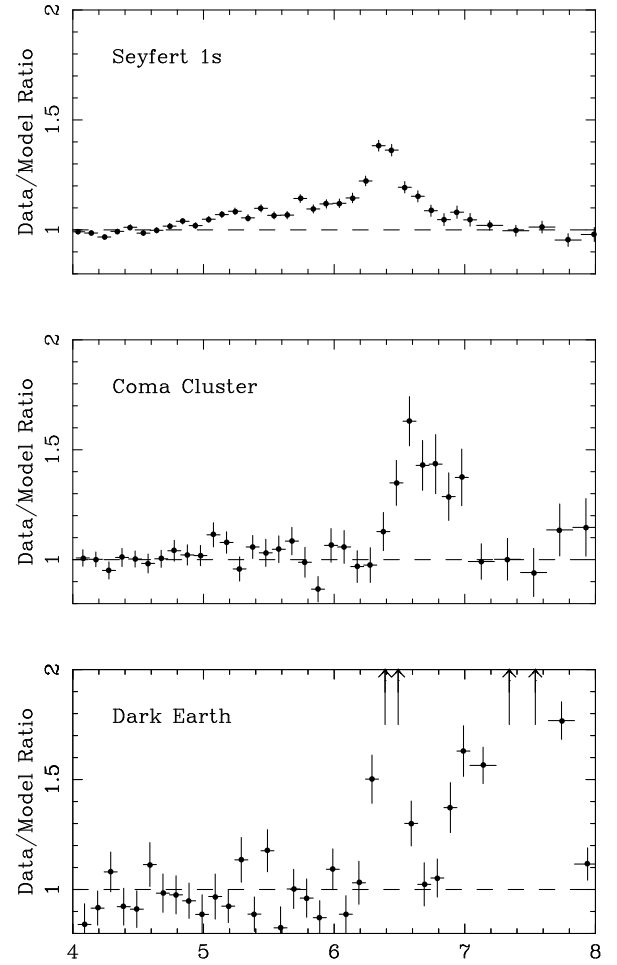
disk, as discussed by Matt, Perola, & Piro (1991), and is therefore supportive of the disk model. Histograms of i and q are shown in Figure 7.

Likelihood analysis reveals no evidence for a significant dispersion in the values of q obtained in our fits, which suggests a common geometry for the sources. However, our conservative error prescription and the assumption that the 68% confidence limit equate to a 1 σ error bar make it difficult to rule out such a hypothesis based on this analysis. A more sensitive method of determining whether or not there are differences in geometry from source to source (in addition to differences in inclination) is to fit the data explicitly with q fixed at the mean value and to compare the χ^2 value so obtained with that when q was left free. We have performed such fits, and these are tabulated in Table 5. It is clear from the fifth column of Table 5, which shows the F-statistic for the addition of q as a free parameter, that many sources prefer a value of q different to the mean. Indeed, 11 of 22 observations and eight of 17 sources show an improvement at >95% confidence. As an ensemble, the reduction in χ^2 is 96.1 for the addition of 22 additional free parameters, significant at >95% confidence. This implies

TABLE 4

DISK-LINE FITS; SCHWARZSCHILD GEOMETRY; FREE EMISSIVITY

Name	Γ_{3-10}	$W_{K\alpha}$	i^a	q^b	$\Delta\chi^{2c}$
Mrk 335	$1.90^{+0.17}_{-0.13}$	230^{+280}_{-170}	23^{+67}_{-23}	$2.2^{+\infty}_{-\infty}$	1.3
Fairall 9	$1.90^{+0.10}_{-0.08}$	350^{+180}_{-130}	45^{+45}_{-21}	$1.9^{+0.5}_{-1.7}$	−0.8
3C 120	$1.87^{+0.06}_{-0.05}$	290^{+110}_{-70}	60^{+30}_{-14}	$2.2^{+0.3}_{-0.5}$	−3.0
NGC 3227	$1.55^{+0.05}_{-0.05}$	210^{+80}_{-80}	20^{+10}_{-10}	$2.0^{+0.4}_{-0.8}$	4.4
NGC 3516	$1.80^{+0.04}_{-0.04}$	330^{+90}_{-80}	27^{+4}_{-5}	$2.7^{+0.7}_{-0.4}$	21.5
NGC 3783(1)	$1.64^{+0.09}_{-0.06}$	370^{+330}_{-110}	21^{+10}_{-7}	$2.5^{+\infty}_{-0.4}$	10.2
NGC 3783(2)	$1.58^{+0.07}_{-0.07}$	430^{+140}_{-120}	32^{+3}_{-13}	$5.2^{+\infty}_{-1.8}$	8.0
NGC 4051	$2.00^{+0.08}_{-0.08}$	460^{+130}_{-230}	33^{+5}_{-13}	$4.4^{+\infty}_{-2.1}$	13.0
NGC 4151(2)	$1.43^{+0.14}_{-0.13}$	190^{+90}_{-50}	18^{+3}_{-8}	$2.0^{+0.4}_{-2.0}$	3.9
NGC 4151(4)	$1.36^{+0.11}_{-0.11}$	550^{+90}_{-120}	33^{+2}_{-8}	$5.0^{+1.9}_{-1.3}$	19.8
NGC 4151(5)	$1.56^{+0.08}_{-0.09}$	320^{+70}_{-60}	17^{+6}_{-5}	$2.8^{+0.4}_{-0.3}$	28.5
Mrk 766	$2.13^{+0.11}_{-0.08}$	610^{+210}_{-200}	35^{+2}_{-4}	$3.7^{+1.9}_{-1.0}$	7.9
NGC 4593	$1.83^{+0.08}_{-0.07}$	240^{+140}_{-140}	45^{+45}_{-45}	$2.2^{+0.7}_{-\infty}$	−0.3
MCG −6-30-15(1)	$2.04^{+0.07}_{-0.06}$	430^{+160}_{-160}	33^{+4}_{-4}	$3.1^{+1.1}_{-0.6}$	7.8
MCG −6-30-15(2)	$1.91^{+0.08}_{-0.06}$	450^{+140}_{-140}	34^{+3}_{-5}	$4.2^{+2.0}_{-1.1}$	3.0
IC 4329A	$1.72^{+0.03}_{-0.03}$	150^{+60}_{-40}	22^{+15}_{-22}	$2.1^{+0.4}_{-1.0}$	2.6
NGC 5548	$1.79^{+0.05}_{-0.05}$	200^{+70}_{-90}	47^{+43}_{-41}	$1.9^{+0.6}_{-0.7}$	−0.6
Mrk 841(1)	$1.95^{+0.14}_{-0.13}$	510^{+260}_{-220}	27^{+7}_{-8}	$2.6^{+6.0}_{-2.8}$	6.4
Mrk 841(2)	$1.62^{+0.16}_{-0.13}$	500^{+310}_{-290}	38^{+2}_{-12}	$10^{+\infty}_{-\infty}$	3.6
NGC 6814(1)	...	...	...	...	...
Mrk 509	$1.81^{+0.11}_{-0.07}$	170^{+160}_{-90}	41^{+49}_{-32}	$2.1^{+0.7}_{-2.0}$	−1.4
NGC 7469(2)	$1.80^{+0.10}_{-0.09}$	210^{+310}_{-130}	19^{+71}_{-19}	$1.8^{+1.0}_{-\infty}$	−1.8
MCG −2-58-22	$1.60^{+0.09}_{-0.11}$	160^{+440}_{-80}	71^{+19}_{-71}	$-10^{+15}_{-\infty}$	0.3

NOTE.—Absorption is by Galactic N_H only, except in the case of NGC 4151, where the column was left free. Error bars on the fit parameters are 68% confidence limits for four interesting parameters ($\Delta\chi^2 = 4.7$).

[a] Inclination of the disk to the line of sight.

[b] The emissivity varies as R^{-q}.

[c] Difference in χ^2 compared to the broad-line fit ($\chi^2_{BL} - \chi^2_S$).

that for this model, the differences in line profiles cannot be accounted for solely by difference in inclination; assuming that the whole of the emission line arises in an accretion disk, we infer that the X-ray source/accretion disk geometry is different from source to source.

The above model assumes that the line profile consists of emission integrated over a range of radii, each of which gives rise to a characteristic line shape. Variations in q correspond to different weightings over the disk. An alternative explanation for the range of observed profiles is that the emission is dominated by a single radius in each source but that this characteristic radius is different in each case. In order to investigate this possibility, we have repeated the disk-line model, but setting $R_i = R_o$ and allowing that radius to be free. q is clearly irrelevant in this case. The χ^2 values for these fits are shown in Table 8. For the sample as
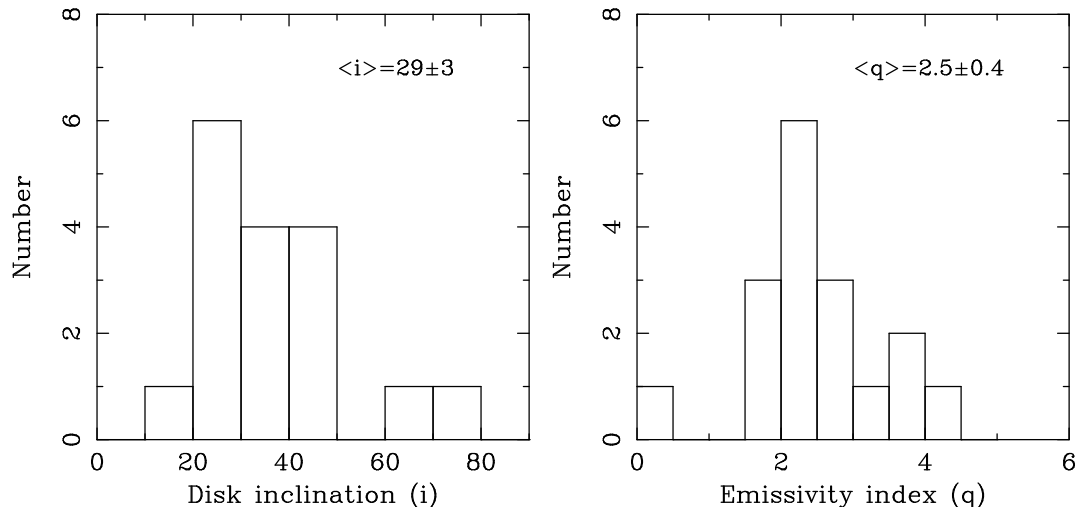

FIG. 6.—Histograms of the parameters from the disk-line fits to the *ASCA* data (see Table 4). *Left*: inclination i; *right*: index of the emissivity function q (see text). The spectra show a significant spread of q, which parameterizes the geometry of the system, which indicates that this may change from source to source.
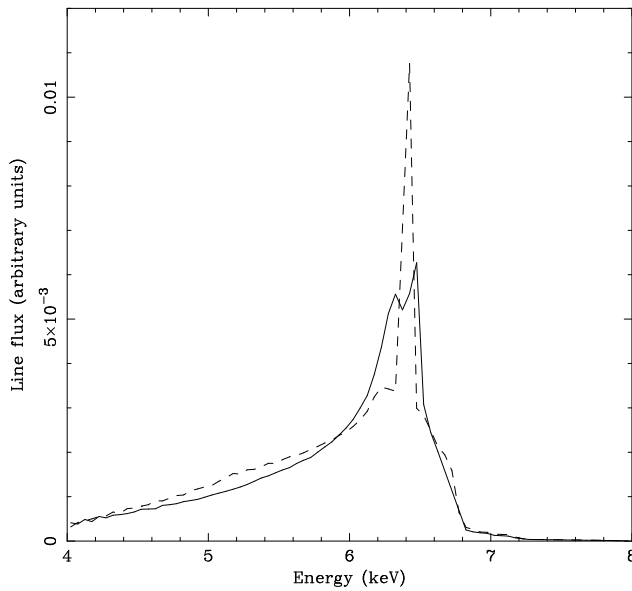
FIG. 7.—Summed model profiles for the sample. The solid line shows the pure disk-line model (Table 4), which is very similar in shape to the data shown in Fig. 4. The dashed line shows the effects of a narrow component. With the resolution of the *ASCA* detectors, it is difficult to state unequivocally whether or not such a component is present. However, including a narrow line has little effect on the disk-line profile.

4.1.1. *Rest Energy of the Line*

In the presence of substantial gravitational and Doppler effects inferred above, the energy derived from a Gaussian fit may not reflect the true rest energy of the line. For example, it is conceivable that gravitational redshift might cause a line that was originally helium-like, with an energy of 6.7 keV, to appear at a lower energy. Given the remarkable consistency of our Gaussian fits with an energy of 6.4 keV and the lack of any strong emission above that energy (Fig. 4), this seems rather contrived. As shown by Matt et al. (1992), for an ensemble of disk lines, the mean energy always lies close to the rest energy, for a variety of emissivity laws. This is due to the fact that the peak energy is dominated by the low-inclination profiles, which are of highest intensity (George & Fabian 1991). We have investigated this further by constructing summed model profiles for an ensemble of accretion disks with inclinations distributed uniformly in cos i. For $q < 3$, the peak energy for the ensemble is redshifted by $<1\%$ of the rest energy. Therefore, unless the emission originates entirely within the central regions, the peak energy in Figure 4 strongly indicates a near-neutral origin for the emission line. This is further illustrated in Figure 7, which shows the summed model profile for the disk-line fits shown in Table 4.

Nonetheless, we have gone on to explore whether our observed profiles are consistent with a helium-like line distorted by the gravitational and Doppler effects in the inner disk. Our first test was with a model identical to that used in the fits of Table 4, i.e., $R_i = 6$, $R_o = 1000$, q and i free, but with the energy of the disk line fixed at 6.7 keV in the rest frame. These fits were considerably worse than with a 6.4 keV line. The total χ^2 was 16,737.2 for 16,973 d.o.f., com-

a whole, they are considerably worse than those with a range of radii with an increase in χ^2 of 106.5 for the same number of degrees of freedom. In only two observations is there an appreciable improvement (i.e., a significant *reduction* in χ^2), NGC 4051 and MCG -6-30-15(1).

TABLE 5

DISK-LINE FITS; SCHWARZSCHILD GEOMETRY; $q = 2.5$

Name	Γ_{3-10}	$W_{K\alpha}$	i	F_1[a]	χ^2_{S25}/d.o.f
Mrk 335	$1.92^{+0.14}_{-0.11}$	280^{+160}_{-150}	24^{+13}_{-24}	0.2	227.9/252
Fairall 9	$1.91^{+0.08}_{-0.07}$	390^{+130}_{-120}	32^{+12}_{-8}	3.8	623.3/610
3C 120	$1.89^{+0.05}_{-0.04}$	350^{+90}_{-100}	59^{+10}_{-13}	3.8	852.7/950
NGC 3227	$1.56^{+0.04}_{-0.05}$	260^{+60}_{-60}	23^{+8}_{-6}	6.6	879.9/920
NGC 3516	$1.80^{+0.03}_{-0.04}$	290^{+50}_{-40}	26^{+4}_{-4}	1.4	994.0/1004
NGC 3783(1)	$1.64^{+0.05}_{-0.05}$	370^{+70}_{-70}	21^{+5}_{-5}	0.0	771.4/788
NGC 3783(2)	$1.55^{+0.06}_{-0.05}$	250^{+60}_{-70}	9^{+11}_{-9}	10.6	694.3/743
NGC 4051	$1.97^{+0.06}_{-0.06}$	310^{+80}_{-110}	27^{+7}_{-11}	3.1	660.9/657
NGC 4151(2)	$1.41^{+0.14}_{-0.12}$	260^{+60}_{-50}	20^{+5}_{-5}	5.6	758.2/694
NGC 4151(4)	$1.52^{+0.08}_{-0.07}$	290^{+50}_{-40}	21^{+5}_{-6}	6.1	1343.8/1400
NGC 4151(5)	$1.60^{+0.07}_{-0.07}$	250^{+40}_{-30}	15^{+4}_{-5}	7.4	1275.1/1227
Mrk 766	$2.09^{+0.08}_{-0.07}$	440^{+110}_{-120}	35^{+5}_{-5}	9.2	570.7/682
NGC 4593	$1.84^{+0.06}_{-0.06}$	280^{+120}_{-100}	45^{+12}_{-11}	1.1	825.5/868
MCG -6-30-15(1)......	$2.02^{+0.05}_{-0.05}$	320^{+70}_{-100}	34^{+5}_{-5}	4.5	910.8/845
MCG -6-30-15(2)......	$1.87^{+0.06}_{-0.05}$	260^{+100}_{-80}	33^{+8}_{-25}	14.4	809.2/802
IC 4329A	$1.72^{+0.03}_{-0.02}$	180^{+40}_{-30}	26^{+7}_{-8}	4.1	1289.1/1249
NGC 5548	$1.79^{+0.05}_{-0.04}$	220^{+90}_{-60}	39^{+10}_{-11}	4.5	973.0/1000
Mrk 841(1)	$1.95^{+0.10}_{-0.11}$	500^{+140}_{-150}	27^{+6}_{-6}	0.1	364.8/368
Mrk 841(2)	$1.61^{+0.12}_{-0.11}$	250^{+160}_{-160}	30^{+9}_{-15}	4.4	181.4/203
NGC 6814(1)	...	...	...	...	...
Mrk 509	$1.81^{+0.06}_{-0.05}$	210^{+120}_{-100}	40^{+48}_{-24}	2.0	809.4/894
NGC 7469(2)	$1.86^{+0.10}_{-0.09}$	370^{+180}_{-180}	45^{+11}_{-29}	1.7	500.7/451
MCG -2-58-22	$1.62^{+0.11}_{-0.08}$	310^{+170}_{-170}	41^{+10}_{-15}	0.5	406.8/388

NOTE.—Absorption is by Galactic N_H only, except in the case of NGC 4151, where the column was left free. Error bars on the fit parameters are 68% confidence limits for three interesting parameters ($\Delta\chi^2 = 3.5$).

[a] F statistic for the addition of q as a free parameter.

pared to 16,627.3 in the near-neutral case. We infer the latter to be >1000 times more likely (Table 8). We have investigated whether this might be due to our assumption of $R_o = 1000$. At large radii, the lack of any significant gravitational or Doppler shifts results in emission close to the rest energy of the line, yet we observe little emission around 6.7 keV (Figs. 3 and 4). Relaxing the constraint on R_o with the helium-like disk line does improve the fits. However, these fits were still slightly worse (total $\chi^2 = 16,633.2$) than those with the 6.4 keV line and a fixed outer radius (total $\chi^2 = 16,628.2$), despite the additional 22 free parameters. However, examination on a case-by-case basis suggests that 3C 120 shows the most marked difference in χ^2. Removal of that outlier would leave the 6.7 keV/free R_o fits showing a slight improvement over those at 6.4 keV/fixed R_o, but not a significant one.

As a further test, we have allowed R_o to be free in the 6.4 keV fits for comparison with the helium-like model. Our suspicion that R_o could not be constrained by these data was largely confirmed by this analysis, with only four observations, NGC 4051, NGC 4151(2), MCG -6-30-15(1), and Mrk 841(1), showing a significant improvement at >95% confidence. The lack of other detections is likely owing primarily to signal-to-noise ratio, the degeneracies inherent in the disk-line models, and the fact that the bulk of the line emission is produced in the central regions. The total χ^2 for those fits was 16,597.0, which indicates that a 6.4 keV line is >1000 times more likely (Table 8) than a 6.7 keV line, even if the outer radius is left free. That conclusion holds even if 3C 120 is removed from consideration.

Relaxing the constraint on the inner radius is unlikely to improve the fits that assume helium-like iron, as we have fixed the inner radius at the last stable orbit in the Schwarzschild metric. This maximizes the gravitational effects, which would tend to bring any highly ionized emission closer to the observed values.

For the four line models tested thus far (narrow Gaussian, broad Gaussian, disk line with fixed R_o, and disk line with free R_o), we have shown that a 6.7 keV line is strongly disfavored. However, this analysis does not preclude the possibility that more complex models can be constructed that conspire to produce an apparent rest energy of 6.4 keV. Particularly, we have assumed that the line can be described by a single component. We now explore the possibility that an additional, narrow line is present.

4.1.2. Narrow-Line Contribution

It is possible that there is a contribution to the emission line from another region. Differing relative contributions from that region and the disk could then confuse our results from the disk-line fits. A promising candidate is the obscuring torus hypothesized in Seyfert 1/2 unification schemes, which could produce a significant contribution in some circumstances (Krolik & Kallman 1987; Ghisselini, Haardt, & Matt 1993; Krolik, Madau, & Zycki 1993). A relatively narrow line might also be produced from the optical "broad-line" region or even the warm absorber.

We have tested for the presence of such a feature by adding a narrow Gaussian, at a rest energy of 6.4 keV to the disk-line models described in Table 4. This provided a significant improvement in the fit for six observations: NGC 3516, NGC 3783(1), NGC 4151(2, 4, 5), and NGC 5548. The improvement for the ensemble is $\Delta\chi^2 = 68.9$ for the 22 degrees of freedom, which is formally highly significant. The

improvement is primarily due to NGC 4151—without that source the improvement for the sample would not be significant ($\Delta\chi^2 = 32.3$ for 19 degrees of freedom). This is noteworthy, as NGC 4151 is the only heavily absorbed source in our sample; conceivably the line-of-sight column could be contributing to the emission line in this case (see Weaver et al. 1994 and Yaqoob et al. 1995 for detailed discussion of the emission line in NGC 4151). In the other cases in which the narrow line provides a significant improvement, this may simply reflect the fact that we have overrestricted the parameter space for the disk-line model. Apparently, there is no requirement for a narrow-line contribution in the majority of our sources, although the upper limits are not restrictive (typically ~ 100 eV, consistent with predictions for the torus; Ghisselini et al. 1993). The mean equivalent width of the narrow component for the sample is only ~ 30 eV.

Even if there is such a narrow component, it has little effect on our conclusions regarding the remainder of the line. This is illustrated in Figure 7, which shows the summed model profiles with and without the narrow line. To quantify the changes, we show in Figure 8 the change in the disk-line parameters ($W_{K\alpha}$, i, q) when the narrow line is
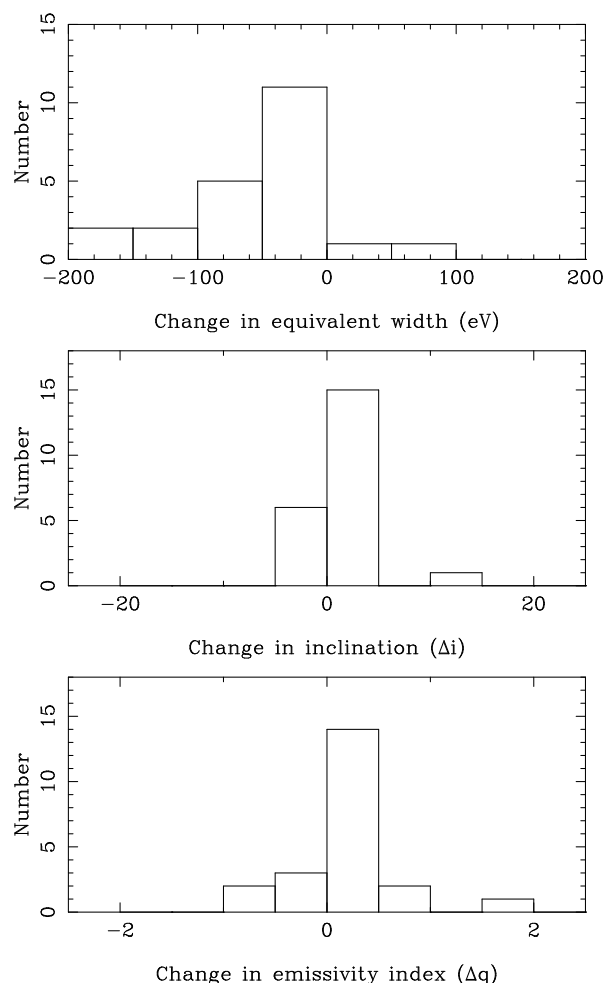

Fig. 8.—Change in the disk-line parameters when a narrow Gaussian, with energy fixed at 6.4 keV, is introduced into the fit. There is a small reduction in the equivalent width (*top panel*) corresponding roughly to the equivalent width of the narrow line (with a mean ~ 30 eV). i (*middle panel*) is largely unchanged by the narrow component, and the mean q (*bottom panel*) increases insignificantly, to 2.8.

added to the model. Obviously, the equivalent width of the disk line decreases when the narrow line is added, but typically only by a few tens of eV. Their effect on the inclinations is negligible; our fits are driven to low inclinations by the lack of significant blue flux, which is not changed by the narrow component. There is a small effect on the emissivity index, with the mean value of q from the disk-line–plus–narrow-line fits being $q = 2.8$, slightly steeper than that without the narrow line, but not significantly so. We have also explored whether the presence of a narrow line can explain the *apparent* difference in geometries implied by the range of q values in Table 4.

Fixing q at the mean value of 2.8 resulted a significantly worse fit in nine of 22 of the observations. Therefore, despite the possible contribution from a molecular torus, or other near-neutral plasma with low velocity, we still conclude that either the geometry of the X-ray source and/or the material that produces the broad, skewed line, differs from source to source.

The one conclusion that does depend critically on the presence or absence of a narrow line is that regarding the rest energy of the disk line. We showed above that a near-neutral origin is considerably more likely than a helium-like line if the entire emission line arises from the disk. In the presence of a narrow line, we can no longer constrain the energy. We find the fits with a 6.4 keV disk line are not significantly better than with a helium-like line, if we allow a narrow line of typical equivalent width ~40 eV at 6.4 keV. This is not surprising, as the main constraint on the rest energy of the disk line comes from the energy of the peak, which in this case is modeled with the narrow line. However, given the lack of conclusive evidence for a narrow-line component in addition to the disk line, a rest energy of 6.4 keV must still be considered more likely, and we have assumed such an energy in the fits described below.

4.1.3. *Effects of the Reflection Continuum*

We next explored the effects of Compton reflection on the spectral parameters. As mentioned in the Introduction, the reflection continuum is commonly observed in the *Ginga* spectra (NP94) and is expected if the material that produces the emission line is optically thick (Lightman & White 1988; George & Fabian 1991; Matt et al. 1991). This is almost certainly the case, given the high equivalent widths.

Although the reflection component is expected to be relatively weak in the *ASCA* band, it may have some influence on the derived line and continuum parameters (see, e.g., Mushotzky et al. 1995; Weaver et al. 1995; Cappi et al. 1996). We therefore added a reflection component to the power-law and disk-line, to investigate the possible effects on these parameters. We employed a model assuming the abundances and cross sections of Morrison & McCammon (1983) and elastic scattering, following Basko (1978). The fact that the *ASCA* spectra extend only to ~10 keV makes the latter approximation reasonable and computationally expedient. We assumed the reflection spectrum from a neutral slab subtending a solid angle of 2π sr at an X-ray source located above the slab. Fits allowing the normalization of the reflection component to be free confirmed our suspicions that typically the reflection continuum can be neither detected nor constrained for these low-redshift AGNs, even when all four instruments are employed. However, our hypothesis is that the line arises by fluores-

cence in an optically thick accretion disk. Simple atomic physics then dictates that the fluorescence must be accompanied by a Compton-scattered continuum.

We have therefore repeated our fits with the disk line, including a fixed reflection component, assuming an inclination as derived from the disk-line model, and an isotropic X-ray source. Note that these fits have no additional free parameters. Including such a component can, in principle, allow additional constraint to be placed on the disk inclination and may affect the disk-line parameters. However, in practice the constraints were no better than without the reflection component included. The mean values of q, i, and $W_{K\alpha}$ (Table 9) were all consistent in these fits compared to those when a pure power-law continuum was used. We did find that the line equivalent width tended to be systematically lower, however, with a mean value of 230 ± 60 eV with reflection included (see Table 9; cf. 290 ± 50 eV without reflection). The reflection component also affects our determination of the continuum (see below). Including the reflection component in the fit resulted in a reduction of the total χ^2 (i.e., for all sources) of 43.9, which implies that for the sample as a whole, the reflection model is considerably more likely than a simple power law (Table 8).

4.2. *Kerr Model*

The previous section has demonstrated that relativistic effects in an accretion disk orbiting a Schwarzschild black hole provide a most agreeable explanation for the line profiles. Those fits suggest that the emission is concentrated close to the central black hole. In such an extreme environment, the details of the black hole metric may even become important. Laor (1991) has presented line profiles for a maximally rotating black hole in the Kerr metric. It was indeed demonstrated that substantial differences in the line profile result, owing primarily to the fact that the innermost stable orbit is closer to the central point mass ($1.23R_g$) and hence the gravitational and Doppler effects are more intense.

We have tested such a model on our data including the reflection component, as described above. This time, we have fixed the inner radius at the last stable orbit for a Kerr hole. We fix the outer radius at $400R_g$, the maximum value allowed in the current implementation of this model in XSPEC. The parameters for the Schwarzschild model are given in Table 6, while the parameters for the Kerr model are tabulated in Table 7. The χ^2 for the Kerr model fits (Table 8) are remarkably similar to those obtained with the Schwarzschild model given in Table 6. The total χ^2 values imply that the Schwarzschild model is ~3 times more likely than the Kerr model, but we do not consider this to be statistically significant. The similarity is probably a consequence of the fact that our fits prefer a relatively low inclination angle. The best-fitting line profiles assuming each metric are shown in Figure 9 for two sources with well-defined profiles. They are indeed rather similar, but the Kerr models have a more pronounced red wing, owing to the increased gravitational redshift within $6R_g$. The mean parameter values for the Kerr fits are entirely consistent with those obtained for the Schwarzschild model (Table 9).

We conclude that a Kerr black hole is not required by our data. Higher resolution and signal-to-noise ratio are required to determine the spin of the black hole definitively.

TABLE 6
Disk-Line Fits; Schwarzschild Geometry; with Reflection

Name	Γ_{3-10}	$W_{K\alpha}$	i	q	$\Delta\chi^2$ [a]	Flux[b]
Mrk 335	$2.05^{+0.14}_{-0.23}$	230^{+310}_{-190}	22^{+68}_{-22}	$2.3^{+\infty}_{-\infty}$	1.1	0.95 ± 0.12
Fairall 9	$2.02^{+0.10}_{-0.18}$	320^{+240}_{-110}	46^{+44}_{-27}	$1.9^{+0.5}_{-2.1}$	0.6	2.05 ± 0.27
3C 120	$1.97^{+0.06}_{-0.14}$	260^{+240}_{-70}	60^{+30}_{-13}	$2.3^{+0.4}_{-0.6}$	0.0	4.69 ± 0.61
NGC 3227	$1.67^{+0.06}_{-0.05}$	190^{+80}_{-60}	20^{+8}_{-14}	$2.0^{+0.5}_{-1.0}$	3.9	2.64 ± 0.33
NGC 3516	$1.93^{+0.04}_{-0.04}$	320^{+120}_{-90}	27^{+6}_{-7}	$2.8^{+\infty}_{-0.4}$	-2.5	6.82 ± 1.03
NGC 3783(1)	$1.77^{+0.08}_{-0.06}$	590^{+130}_{-140}	35^{+2}_{-18}	$8.5^{+\infty}_{-4.6}$	2.9	5.12 ± 0.67
NGC 3783(2)	$1.70^{+0.06}_{-0.07}$	400^{+120}_{-120}	32^{+3}_{-15}	$6.4^{+\infty}_{-2.6}$	2.0	6.12 ± 0.80
NGC 4051	$2.11^{+0.08}_{-0.08}$	420^{+160}_{-210}	34^{+3}_{-14}	$5.1^{+\infty}_{-2.6}$	0.6	2.13 ± 0.28
NGC 4151(2)	$1.60^{+0.13}_{-0.13}$	150^{+90}_{-70}	17^{+12}_{-17}	$1.8^{+0.6}_{-\infty}$	5.6	24.3 ± 3.1
NGC 4151(4)	$1.54^{+0.10}_{-0.11}$	490^{+100}_{-90}	33^{+2}_{-18}	$5.4^{+3.0}_{-1.5}$	2.3	27.8 ± 3.6
NGC 4151(5)	$1.72^{+0.09}_{-0.08}$	290^{+70}_{-60}	17^{+5}_{-5}	$2.9^{+0.3}_{-0.3}$	1.1	32.6 ± 4.2
Mrk 766	$2.25^{+0.10}_{-0.09}$	580^{+200}_{-200}	34^{+3}_{-3}	$3.9^{+2.9}_{-1.0}$	1.4	1.95 ± 0.25
NGC 4593	$1.91^{+0.09}_{-0.05}$	90^{+70}_{-50}	0^{+79}_{-0}	$1.5^{+1.3}_{-\infty}$	5.1	3.38 ± 0.44
MCG -6-30-15(1)	$2.16^{+0.06}_{-0.07}$	400^{+150}_{-220}	33^{+3}_{-5}	$3.4^{+1.3}_{-0.8}$	3.2	4.69 ± 0.61
MCG -6-30-15(2)	$2.03^{+0.07}_{-0.07}$	410^{+140}_{-140}	34^{+3}_{-6}	$4.4^{+3.0}_{-1.1}$	-0.4	3.83 ± 0.50
IC 4329A	$1.84^{+0.03}_{-0.03}$	120^{+60}_{-40}	17^{+14}_{-17}	$2.1^{+2.8}_{-1.1}$	3.3	8.12 ± 1.06
NGC 5548	$1.89^{+0.04}_{-0.05}$	80^{+30}_{-30}	0^{+76}_{-0}	$-9.0^{+11.5}_{-\infty}$	6.2	4.71 ± 0.61
Mrk 841(1)	$2.07^{+0.13}_{-0.13}$	470^{+430}_{-220}	27^{+7}_{-9}	$2.6^{+\infty}_{-1.3}$	1.0	1.29 ± 0.17
Mrk 841(2)	$1.74^{+0.16}_{-0.13}$	440^{+310}_{-280}	38^{+2}_{-16}	$10^{+\infty}_{-\infty}$	-1.7	1.07 ± 0.14
NGC 6814(1)	...	...	...	...	...	0.13 ± 0.02
Mrk 509	$1.92^{+0.06}_{-0.07}$	110^{+100}_{-70}	27^{+63}_{-27}	$2.2^{+1.2}_{-\infty}$	1.6	4.58 ± 0.59
NGC 7469(2)	$1.91^{+0.09}_{-0.08}$	120^{+60}_{-60}	0^{+89}_{-0}	$-9.0^{+10.7}_{-\infty}$	4.1	2.78 ± 0.36
MCG -2-58-22	$1.70^{+0.16}_{-0.18}$	140^{+160}_{-80}	46^{+44}_{-46}	$-4.8^{+\infty}_{-\infty}$	2.0	1.48 ± 0.19

NOTE.—Absorption is by Galactic N_H only, except in the case of NGC 4151, where the column was left free. Error bars on the fit parameters are 68% confidence limits for four interesting parameters ($\Delta\chi^2 = 4.7$).

[a] Reduction in χ^2 relative to the model with a Schwarzschild disk line and power law, i.e. $\chi^2_S - \chi^2_{SR}$.

[b] Flux in the 2–10 keV band in units of 10^{-11} ergs cm^{-2} s^{-1}, based on the model described in this table, but corrected for absorption. The error bar corresponds to the absolute calibration of the SIS detectors of $\sim 13\%$.

TABLE 7
Disk-Line Fits; Kerr Geometry; with Reflection

Name	Γ_{3-18}	$W_{K\alpha}$	i	q	$\Delta\chi^2$ [a]
Mrk 335	$2.04^{+0.15}_{-0.24}$	250^{+390}_{-220}	22^{+68}_{-22}	$2.2^{+1.2}_{-\infty}$	-0.6
Fairall 9	$1.93^{+0.14}_{-0.10}$	360^{+200}_{-150}	89^{+1}_{-49}	$1.3^{+0.9}_{-7.2}$	-0.1
3C 120	$2.01^{+0.05}_{-0.04}$	670^{+90}_{-120}	88^{+2}_{-1}	$2.7^{+0.4}_{-0.2}$	5.3
NGC 3227	$1.67^{+0.05}_{-0.05}$	180^{+110}_{-70}	21^{+7}_{-21}	$1.8^{+0.6}_{-5.6}$	-1.8
NGC 3516	$1.92^{+0.04}_{-0.03}$	380^{+90}_{-90}	26^{+3}_{-4}	$2.6^{+0.3}_{-0.2}$	4.9
NGC 3783(1)	$1.77^{+0.06}_{-0.06}$	550^{+190}_{-190}	26^{+5}_{-5}	$2.7^{+0.3}_{-0.4}$	-1.6
NGC 3783(2)	$1.67^{+0.08}_{-0.07}$	630^{+360}_{-390}	40^{+12}_{-40}	$3.9^{+1.7}_{-0.9}$	-0.8
NGC 4051	$2.10^{+0.08}_{-0.07}$	440^{+340}_{-200}	25^{+12}_{-4}	$2.8^{+0.8}_{-0.5}$	0.2
NGC 4151(2)	$1.60^{+0.13}_{-0.13}$	120^{+40}_{-30}	9^{+18}_{-9}	$-10^{+12.1}_{-\infty}$	-3.2
NGC 4151(4)	$1.58^{+0.14}_{-0.14}$	470^{+190}_{-170}	24^{+5}_{-7}	$2.8^{+0.3}_{-0.4}$	-0.6
NGC 4151(5)	$1.57^{+0.17}_{-0.15}$	540^{+220}_{-210}	21^{+5}_{-11}	$3.0^{+0.3}_{-0.3}$	0.0
Mrk 766	$2.25^{+0.10}_{-0.10}$	860^{+470}_{-370}	36^{+8}_{-7}	$3.0^{+0.8}_{-0.4}$	-0.5
NGC 4593	$1.91^{+0.16}_{-0.14}$	90^{+200}_{-50}	0^{+56}_{-0}	$-0.6^{+3.2}_{-\infty}$	-0.5
MCG -6-30-15(1)	$2.15^{+0.07}_{-0.06}$	480^{+260}_{-200}	34^{+5}_{-6}	$2.8^{+0.5}_{-0.5}$	-0.5
MCG -6-30-15(2)	$2.02^{+0.08}_{-0.07}$	730^{+540}_{-280}	34^{+16}_{-9}	$3.3^{+1.9}_{-0.4}$	2.9
IC 4329A	$1.84^{+0.03}_{-0.03}$	110^{+80}_{-40}	10^{+13}_{-10}	$1.8^{+0.7}_{-5.8}$	0.5
NGC 5548	$1.89^{+0.04}_{-0.04}$	90^{+120}_{-40}	10^{+80}_{-10}	$0.5^{+1.9}_{-\infty}$	-1.7
Mrk 841(1)	$2.07^{+0.14}_{-0.11}$	590^{+390}_{-270}	26^{+8}_{-5}	$2.5^{+0.5}_{-0.7}$	-1.1
Mrk 841(2)	$1.59^{+0.16}_{-0.13}$	140^{+120}_{-110}	90^{+0}_{-90}	$-10^{+16.3}_{-\infty}$	-2.9
NGC 6814(1)	...	...	...	...	...
Mrk 509	$1.84^{+0.14}_{-0.09}$	230^{+340}_{-140}	89^{+1}_{-89}	$1.8^{+1.0}_{-6.0}$	0.8
NGC 7469(2)	$1.93^{+0.09}_{-0.09}$	170^{+230}_{-100}	20^{+70}_{-20}	$1.4^{+1.0}_{-\infty}$	-0.2
MCG -2-58-22	$1.72^{+0.09}_{-0.10}$	140^{+120}_{-80}	26^{+64}_{-26}	$-10.0^{+15.3}_{-\infty}$	0.0

NOTE.—Absorption is by Galactic N_H only, except in the case of NGC 4151, where the column was left free. Error bars on the fit parameters are 68% confidence limits for four interesting parameters ($\Delta\chi^2 = 4.7$).

[a] Reduction in χ^2 relative to the model with a Schwarzschild diskline and reflection continuum, i.e. $\chi^2_{SR} - \chi^2_{KR}$.

TABLE 8

COMPARISON OF χ^2 VALUES

Name	χ^2_{BL}	χ^2_{S}	χ^2_{S67}	χ^2_{SS}	χ^2_{SR}	χ^2_{KR}	d.o.f
Mrk 335	227.0	225.7	226.3	225.3	224.6	225.2	251
Fairall 9	618.6	619.4	625.5	626.9	618.8	618.9	609
3C 120	846.3	849.3	868.9	862.7	849.3	844.0	949
NGC 3227	878.0	873.6	890.3	875.9	869.7	871.5	919
NGC 3516..............	1014.1	992.6	994.5	1011.3	995.1	990.2	1003
NGC 3783(1)	781.6	771.4	775.8	771.4	768.5	770.1	787
NGC 3783(2)	692.4	684.4	683.1	693.2	682.4	683.2	742
NGC 4051	670.8	657.8	656.4	645.0	657.2	657.0	656
NGC 4151(2)	755.9	752.1	763.8	757.1	746.5	749.7	693
NGC 4151(4)	1357.7	1337.9	1331.6	1347.5	1335.6	1336.2	1399
NGC 4151(5)	1295.9	1267.4	1280.9	1282.1	1266.3	1266.3	1226
Mrk 766	570.9	563.0	562.2	577.2	563.0	563.5	681
NGC 4593..............	824.2	824.5	831.7	824.5	819.4	819.9	867
MCG -6-30-15(1)......	913.8	906.0	905.5	898.6	902.8	903.3	844
MCG -6-30-15(2)......	797.7	794.7	792.1	797.9	795.1	792.2	801
IC 4329A	1287.5	1284.9	1296.2	1306.9	1281.6	1281.1	1248
NGC 5548	968.0	968.6	974.2	974.1	962.4	964.1	999
Mrk 841(1)	371.1	364.7	369.9	359.4	362.3	363.4	367
Mrk 841(2)	181.1	177.5	180.9	181.8	179.2	182.1	202
NGC 6814(1)	...	...	...	...	...	...	
Mrk 509	806.2	807.6	816.7	809.7	806.0	805.2	893
NGC 7469(2)	497.0	498.8	503.3	498.4	494.7	494.9	450
MCG -2-58-22	406.6	406.3	407.4	407.8	404.3	404.3	387

Total Values

	χ^2_{BL}	χ^2_{S}	χ^2_{S67}	χ^2_{SS}	χ^2_{SR}	χ^2_{KR}	d.o.f
Value (-16000)	762.4	628.2	737.2	734.7	584.4	586.3	973
Probability	0.87	0.97	0.90	0.90	0.98	0.98	...

Relative Likelihoods[a]

	χ^2_{BL}	χ^2_{S}	χ^2_{S67}	χ^2_{SS}	χ^2_{SR}	χ^2_{KR}	
χ^2_{BL}	...	$>10^3$	$>10^3$	$>10^3$	$>10^3$	$>10^3$	...
χ^2_{S}	$<10^{-3}$	...	$<10^{-3}$	$<10^{-3}$	$>10^3$	$>10^3$	...
χ^2_{S67}	$<10^{-3}$	$>10^3$	...	0.29	$>10^3$	$>10^3$	...
χ^2_{SS}	$<10^{-3}$	$>10^3$	3.5	...	$>10^3$	$>10^3$	...
χ^2_{SR}	$<10^{-3}$	$<10^{-3}$	$<10^{-3}$	$<10^{-3}$	...	0.39	...
χ^2_{KR}	$<10^{-3}$	$<10^{-3}$	$<10^{-3}$	$<10^{-3}$	2.6	...	...

NOTE.—The subscripts used are as follows: BL, broad Gaussian (Table 3); S, Schwarzschild model (Table 4); S67, Schwarzschild model with a rest energy of 6.7 keV; SS, Schwarzschild model at a single radius; SR, Schwarzschild with reflection (Table 6); KR, Kerr model with reflection (Table 7).

[a] Likelihood of the model in the column heading compared to the row, based on the total χ^2 values.

4.3. The X-Ray Continuum

While our primary goal in considering the 3–10 keV spectra of these Seyfert galaxies was to define the iron-line properties of the sample, these data also allow us to define the continuum in this band. For a number of the emission-line models mentioned above, we have tabulated the mean power-law indices, which are shown in Table 9. As can be seen from this table, the mean power-law slope is not strongly dependent on the *line* model, ranging from $\langle \Gamma_{3-10} \rangle = 1.75$ for a narrow line to $\langle \Gamma_{3-10} \rangle = 1.79$ for a disk-line model. However, although the presence of a reflection continuum causes minimal change in the derived line parameters, there is a substantial effect on the continuum. In the fits tabulated in Table 6, the mean spectral slope when reflection is included is $\langle \Gamma_{3-10} \rangle = 1.91 \pm 0.10$ (Fig. 10; Table 9), $\Delta\Gamma = 0.12$ steeper than with a power-law continuum.

Conceivably there might also be other spectral components that can affect the continuum. The most obvious of these are low-energy absorption and iron K-edge absorption, both of which have been reported for some *Ginga* spectra (NP94). We have tested for the presence of each of these in our sample. Aside from the well-known case of NGC 4151 (for which we have already included an absorption column), we find no evidence for soft X-ray absorption.

This justifies post facto our choice of the 3–10 keV range for determination of the line parameters (note that neutral columns $\lesssim 10^{22}$ cm^{-2} have little effect above 3 keV). Addition of an iron K-edge does provide a significant improvement (at $\sim 95\%$ confidence) in four observations of three sources [NGC 3516—see Fig. 9; NGC 3783(1); NGC 3783(2); and NGC 4151(2)]. A plausible origin for the edge is in the warm absorber mentioned in the Introduction. However, even when such an edge is detected, it has minimal effect on the line and continuum parameters and thus can be disregarded for the purposes of our analysis.

5. COMPARISON WITH PREVIOUS RESULTS

Although a number of the observations presented here have been published previously, detailed discussion of the emission-line properties has been relatively rare. However, where comparisons can be made we find consistency with our fits. Specifically, our results are entirely consistent with those presented by Ptak et al. (1994) for NGC 3227, Mihara et al. (1994) for NGC 4051, Weaver et al. (1994) and Yaqoob et al. (1995) for NGC 4151, Reynolds et al. (1995b) and Tanaka et al. (1995) for MCG -6-30-15, Mushotzky et al. (1995) for IC 4329A and NGC 5548, Guainazzi et al. (1994) for NGC 7469 and MCG -2-58-22 (Weaver et al. 1995). We find some disagreement in interpretation for NGC 3783,
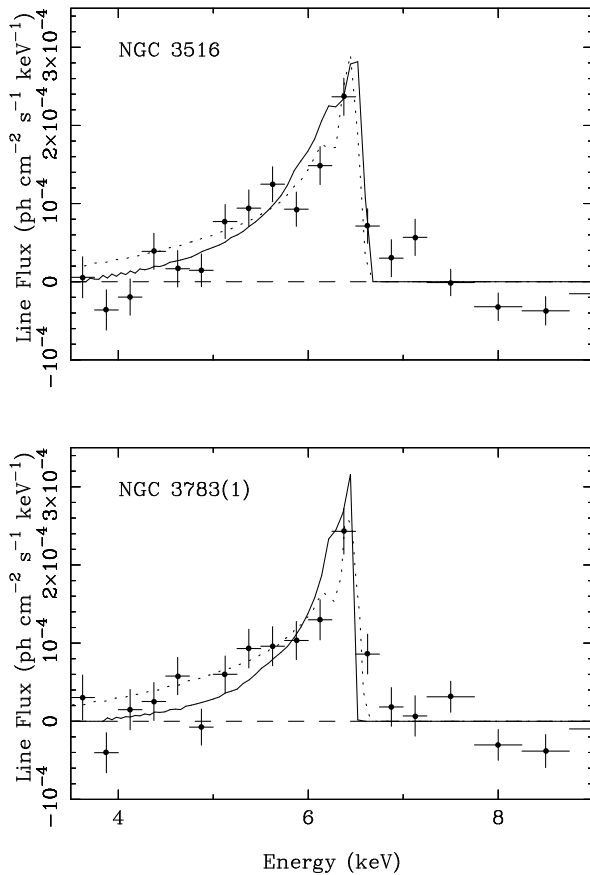
FIG. 9.—Residual profiles for NGC 3516 (*top panel*) and NGC 3227 (*bottom panel*). Data from all four instruments have been combined in bins of 0.25 keV width. The best-fit Schwarzschild (*solid line*) and Kerr (*dotted line*) models are also shown.

where George, Turner, & Netzer (1995) claimed no evidence for broadening of the line. We consider this to be due to the fact that George et al. fixed the photon index in the fit. Similarly, Leighly et al. (1996) claim no evidence for broadening of the line in Mrk 766 but did not allow the energy of the line to vary from 6.4 keV. Figure 3 indicates

both narrow and broad components to the line in Mrk 766. We suggest that Leighly et al. were measuring only the narrow component.

The results for the *ASCA* sample are also remarkably consistent with the lower resolution *Ginga* data. NP94 found a mean energy of 6.37 ± 0.07 keV and equivalent width 140 ± 20 for a "narrow" Gaussian. As mentioned above, the latter is most directly comparable to that of our broad-line fits, given the width of the *Ginga* response, and is entirely consistent with those fits. The mean spectral index from *Ginga* was 1.95 ± 0.05 when the effects of reflection and the warm absorber were accounted for (NP94).

6. SUMMARY OF RESULTS

In this paper, we have found the following:

Emission at iron Kα is detected in all 23 observations of our 18 sources.

The line to be resolved in 80% of the sources, with a mean width corresponding to a FWHM of 47,000 km s^{-1} assuming a Gaussian profile.

The profiles are often asymmetric, with a peak at ~ 6.4 keV in rest-frame and a broad wing extended to the red. The FWZI of the mean line profile corresponds to a velocity of $\sim 0.3c$.

All of the profiles are consistent with that expected from an accretion disk orbiting a central black hole. Both Schwarzschild and Kerr metrics model the data equally well.

A mean inclination of $i \sim 30°$. With a random distribution, we expect a mean of 60°.

An emissivity function of R^{-q} between $R_i = 6R_g$ and $R_o = 1000R_g$, with $q \sim 2.5$. This demonstrates that the line emission is concentrated in the inner disk. However, the data are not consistent with a universal emissivity law.

Assuming the whole of the line arises from the disk, fits with a rest energy of 6.7 keV are strongly disfavored. It is most likely that the line arises by fluorescence in near-neutral material.

No strong evidence exists for a narrow component at 6.4 keV in addition to the disk line, but with upper limits typically ~ 100 eV. The presence or absence of the narrow component affects neither the values of q and i nor the inferred
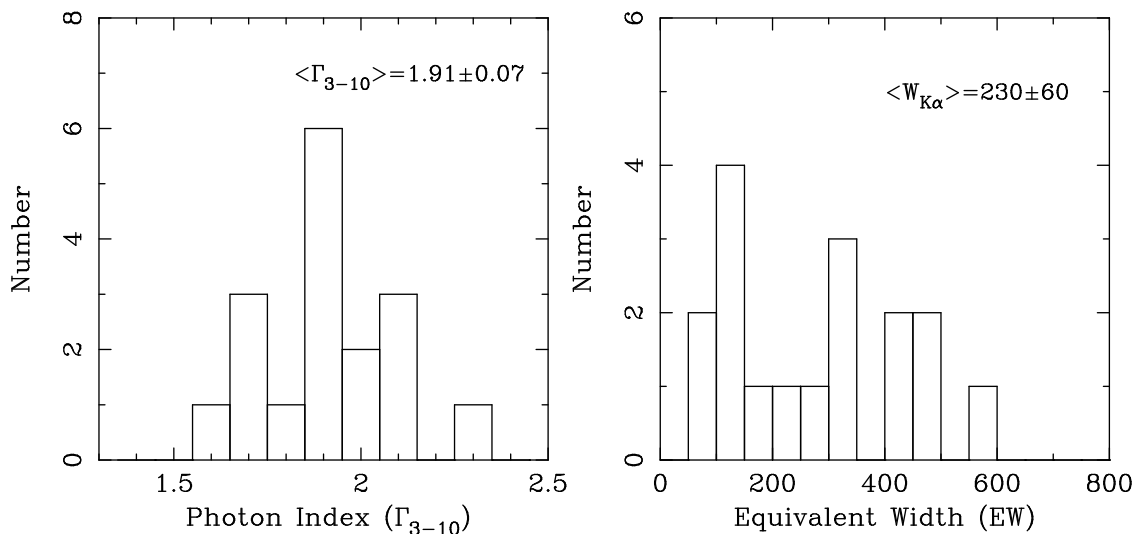

FIG. 10.—Histograms of (*left*) the photon index of the power law, Γ_{3-10}, and (*right*) the line equivalent width, $W_{K\alpha}$ from disk-line–plus–reflection fits to the *ASCA* data (see Table 6). The inclination and emissivity index show negligible change when reflection is included. In contrast, the power-law index is steepened by $\Delta\Gamma = 0.12$, and the mean equivalent width reduces by ~ 50 eV when the effects of reflection are accounted for.

TABLE 9

MEAN PARAMETERS FOR THE SEYFERT 1 GALAXIES

Parameter (1)	Unit (2)	μ^a (3)	$\bar{\mu}^b$ (4)	$\langle \mu \rangle^c$ (5)	σ_i^d (6)
Narrow-Line Fits, 3–10 keV					
Γ_{3-10}	...	1.74 ± 0.14	1.74 ± 0.01	1.75 ± 0.05	0.12 ± 0.04
$E_{K\alpha}$	keV	6.34 ± 0.12	6.36 ± 0.01	6.36 ± 0.02	< 0.06
$W_{K\alpha}$	eV	115 ± 39	98 ± 8	98 ± 12	< 24
Broad-Line Fits, 3–10 keV					
Γ_{3-10}	...	1.80 ± 0.17	1.76 ± 0.02	1.78 ± 0.06	0.13 ± 0.05
$E_{K\alpha}$	keV	6.29 ± 0.14	6.34 ± 0.02	6.34 ± 0.04	< 0.09
$W_{K\alpha}$	eV	290 ± 240	150 ± 20	160 ± 30	< 90
$\sigma_{K\alpha}$	keV	0.40 ± 0.28	0.39 ± 0.06	0.43 ± 0.12	< 0.29
Disk Line, Free q					
Γ_{3-10}	...	1.80 ± 0.17	1.76 ± 0.02	1.79 ± 0.07	0.15 ± 0.05
$W_{K\alpha}$	eV	310 ± 140	280 ± 30	290 ± 50	< 140
i	deg	35 ± 15	29 ± 2	29 ± 3	< 9
q	...	1.9 ± 3.2	2.5 ± 0.2	2.5 ± 0.4	< 0.8
Disk Line, Free q, Reflection					
Γ_{3-10}	...	1.92 ± 0.17	1.88 ± 0.02	1.91 ± 0.07	0.15 ± 0.05
$W_{K\alpha}$	eV	270 ± 160	180 ± 20	230 ± 60	110 ± 50
i	deg	26 ± 17	29 ± 2	29 ± 5	< 11
q	...	1.1 ± 4.5	2.8 ± 0.3	2.8 ± 0.4	< 0.9
Kerr Model, Free q, Reflection					
Γ_{3-10}	...	1.90 ± 0.17	1.88 ± 0.02	1.89 ± 0.07	0.15 ± 0.05
$W_{K\alpha}$	eV	320 ± 230	210 ± 30	270 ± 60	130 ± 60
i	deg	34 ± 28	28 ± 3	28 ± 4	< 8
q	...	1.3 ± 3.1	2.8 ± 0.2	2.8 ± 0.2	< 0.4

NOTE.—Error bars are 68% confidence limits. Upper limits are 90% confidence.
[a] Unweighted mean and standard deviation.
[b] Weighted mean.
[c] Expectation allowing for measurement errors (see text).
[d] Intrinsic dispersion of distribution (see text).

differences in q, but removes our constraints on the rest energy of the disk line.

A Compton-"reflection" component, which is expected to accompany the line, is likely to be present, but does not affect the inferred line profiles.

A mean equivalent width of 230 eV when reflection is included.

The underlying continuum in our sample to be characterized by a power law with a photon index $\Gamma = 1.9$, with a dispersion of 0.15.

7. DISCUSSION

Since the discovery of active galactic nuclei, most workers have assumed that they are powered by accretion onto a black hole. Such a model apparently presents the only reasonable explanation for the observed phenomena (Rees 1984 and references therein). However, as a black hole is not directly observable, one is able to infer its existence only through the influence of its physical properties: mass and spin. The velocities of gas observed at ~0.1 pc from the nucleus of some galaxies strongly indicate the presence of huge masses in the central regions (see, e.g., Ford et al. 1994; Miyoshi et al. 1995), with the only viable model appearing to be a black hole. However, detection of the characteristic relativistic effects of the black hole requires data that probe much smaller scales, closer to the event horizon. The velocities here should begin to approach the speed of light, and, furthermore, the gravitational field of the black hole will cause time-dilation effects resulting in gravitational redshift. In order to measure such phenomena, discrete spectral features are necessary. The characteristic broadening and distortion of those features owing to the relativistic motions represent arguably the most compelling test of the black hole paradigm. The iron Kα profile observed by Tanaka et al. (1995) in MCG −6-30-15 represents strong evidence for such a hypothesis in that object. The similarity of the profile in NGC 4151 (Yaqoob et al. 1995) tempts one to extrapolate this model to Seyfert galaxies as a class. But is such a generalization appropriate?

In this paper, we have presented a uniform analysis of a sample of Seyfert 1 galaxies including MCG −6-30-15 and NGC 4151. We found results consistent with previous work for MCG −6-30-15 and NGC 4151 but have further demonstrated that asymmetric line profiles are widespread. Fits to a specific physical model for the central regions of the AGN, that of an accretion disk orbiting in the Schwarzschild metric, provide significant improvements over a simple Gaussian. This supports the assertion that the line is produced very close to a central black hole. The average emissivity function implies that ~50% of the line emission originates within ~20R_g, and ~80% within ~100R_g. Special and general relativistic effects thus afford a most satisfying explanation for the observed broadening. Furthermore, the lack of any strong blueshifts in our sample argues for a planar geometry, such as a disk (see, e.g., Fabian et al. 1995). However, detailed calculations of the

line profiles expected in other geometries are beyond the scope of this paper.

Detailed interpretation of the line profiles is model dependent. However, the distribution of parameters for the sample can be compared to those predicted by specific disk models. For example, if these Seyfert 1 galaxies were viewed at all inclinations, we would expect a mean of 60° for the sample. Therefore, our disk-line fits imply that we tend to observe the Seyfert 1 galaxies at a more face-on inclination, on average at 30°. This may be reconciled with Seyfert 1/2 unification schemes (see, e.g., Antonucci & Miller 1985). In these models, all Seyfert galaxies are surrounded by a thick, molecular torus that obscures the line of sight in Seyfert 2 galaxies. If the torus axis were aligned with that of the disk, we would not then expect to see any edge-on Seyfert 1 galaxies. The broad lines would be obscured by the torus for lines of sight with $i > i_{op}$, the opening angle of the torus. Based on our mean disk inclination, we would estimate $\cos i_{op} \sim (1 - \cos \langle i \rangle / 2)$, implying an opening angle of $\sim 45°$. This is in excellent agreement with estimates based on the observations of ionization cones (Pogge 1989 and references therein) in the optical. Although our data did not show strong evidence for a narrow emission line—expected from the torus—neither did they exclude a narrow component with the predicted strength (Ghisselini et al. 1993; Krolik et al. 1993). Conclusive evidence requires data with higher spectral resolution and signal-to-noise ratio. However, the presence of a narrow component has little effect on the derived parameters for the disk line, particularly q and i. An alternative explanation for the restricted range in i is that the disk itself—if geometrically thick—obscures the edge-on lines of sight.

Assuming that the disk line accounts for all of the emission at iron Kα, the requirement for a rest energy of 6.4 keV implies that the line arises by fluorescence excited by the power-law continuum. This raises the question as to how the disk can remain relatively neutral when exposed to such intense illumination. The immediate conclusion is that the density of the fluorescing material is extremely high. Photoionized accretion disks have been discussed by Ross & Fabian (1993) and Matt, Fabian, & Ross (1993). For a standard α-disk, we expect a density, n, at $20R_g$, of (Matt et al. 1993):

$$ n = 1.2 \times 10^{15} \frac{\eta_{0.06}^2}{\dot{M}_{0.1}^2 M_8 \alpha_{0.01}} \text{ cm}^{-3} , $$

where $\dot{M} = 0.1\dot{M}_{0.1}$ is the accretion rate in units of the Eddington rate, $M = 10^8 M_8$ is the black hole mass in solar masses, $\eta = 0.06\eta_{0.06}$ is the energy conversion efficiency, and $\alpha = 0.01\alpha_{0.01}$ is the dimensionless viscosity parameter. The ionization parameter is approximately

$$ \xi = \frac{L_X}{nR^2} \sim \frac{L_{44} \dot{M}_{0.1}^2 \alpha_{0.01}}{M_8 \eta_{0.06}^2} , $$

where $L_X = 10^{44} L_{44}$ is the ionizing luminosity. Below $\xi \sim 300$ a rest energy close to 6.4 keV is predicted for the line (Matt et al. 1993). Thus, even in the central regions, we typically expect the mean ionization state for the disk to be low. However, presumably the surface layers, where the bulk of the fluorescence occurs, could be more highly ionized than is indicated by the above relations. Assuming fixed energy fractions between the X-ray and intrinsic disk

emission, we infer that $\xi \propto \dot{M}^3$ and thus that the accretion rate is the dominant parameter in determining the ionization state of the disk. This implies that the $\dot{M}$ values in these Seyfert galaxies are subcritical. Interestingly, for some quasars, in which the accretion rates may be higher, there is evidence that the peak of the emission line is higher, which is indicative of more ionized iron (Nandra et al. 1996).

Our fits to the Schwarzschild model have also shown that the measured line profiles are not compatible with a universal emissivity function, even when the inclination and a possible contribution of a narrow line from another region are allowed to vary. This might be a consequence of slight differences in geometry from source to source. For example, if the true inner and outer radii of the disk are different from those assumed, this can be compensated for in the fit by changing the apparent emissivity function. Alternatively, as we are dealing with a fluorescence line, the line emissivity depends upon the X-ray illumination, which could change from source to source. For example, with a pointlike X-ray source located above the disk, the line profile depends upon the height of the source (Matt et al. 1992). Our data are well fitted by the disk-line model only if we allow the emission to be distributed over a range of radii. Emission at a single radius cannot account for the observed profiles in the majority of cases. This argues against models in which the height of the X-ray source is very small, where only the inner disk is illuminated. Furthermore, models in which the disk presents significant solid angle to the X-ray source only at a small number of radii are difficult to reconcile with our data. One might envisage such a scenario if the X-ray source were at the inner edge of the disk itself or if the very innermost regions of the disk were puffed up by radiation pressure.

A simplistic " one-zone " model for the X-ray source may not be appropriate. A currently popular model is of multiple regions or "hot spots" covering the surface of the disk (see, e.g., Stern et al. 1995). The mean emissivity profile is harder to calculate in such a case, as it depends on the distribution of hot spots within the X-ray producing region and the variation of their density with radius. By observation, we conclude that in such a model, this latter quantity should vary approximately as $R^{-2.5}$. The challenge is now for theoretical models to reproduce such a relationship and, one would hope, relate it to the energy-generation mechanism for the X-rays.

An area where our observational data come into mild conflict with the conventional wisdom regarding disk reflection is that of the line equivalent width. The detailed calculations of George & Fabian (1991) and Matt et al. (1991) predicted a value from the disk of $W_{K\alpha} = 140$ eV for a continuum with $\Gamma = 1.9$ and an inclination of 30°. This is a factor 1.2–2 less than our observed mean of 230 ± 60 eV. An obvious way to resolve this discrepancy is to revise our assumptions about the metal abundances. The required increase in equivalent width can be achieved by an enhancement in the iron abundance of a factor 1.3–3.5 over the values of Morisson & McCammon (1983), which are usually employed (see Fig. 16 of George & Fabian 1991). Indeed, using the updated solar abundances of Anders & Grevesse (1989), Reynolds, Fabian, & Inoue (1995a) find that equivalent widths of ~ 250 eV could be achieved without any enhancement in iron. The possible contribution of ~ 30 eV of a narrow line from another region would also ease this discrepancy somewhat.

The mean iron abundance derived here argues that the material being accreted is relatively metal-rich, consistent with recent broad-line models for quasars (Hamann & Ferland 1993). Since the central regions of most spiral galaxies have similar metallicities, but the abundances drop with increasing radius (McCall, Rybski, & Shields 1985; Shields, Skillman, & Kennicutt 1991), this tends to imply that the accretion fuel is produced by stellar mass loss relatively close to the nucleus and is not brought in from farther out in the galaxy. The required accretion rate is $\dot{M} = 3 \times 10^{-2} L_{44} \eta_{0.06} M_{\odot} \text{ yr}^{-1}$ (here L_{44} represents the accretion luminosity, rather than the ionizing luminosity). The mass-loss rate is expected to be $\dot{M} \sim 10^{-2} M_{10} M_{\odot} \text{ yr}^{-1}$, where M_{10} is the mass of stars in units of $10^{10} M_{\odot}$, which seems plausible.

Our fits have also allowed us to define the continuum shape in the 3–10 keV band. We find a mean slope of ~ 1.8 with a power-law–plus–line model. This lies between the values determined by *HEAO 1* and *EXOSAT* (using a single power law; Mushotzky 1984; Turner & Pounds 1989) and that determined from *Ginga*, where a more complex model was employed, including a warm absorber and reflection. When we include the reflection component in our *ASCA* fits, we find $\Gamma = 1.9$, in excellent agreement with the *Ginga* data, which were arguably more appropriate for continuum determination. These results indicate that the reflection component has a substantial effect on the determination of the continuum using *ASCA* data in the 3–10 keV band but that the warm absorber does not. We

will return to this latter point in Paper III. Our data have implications for the physical models of the X-ray continuum in AGNs. For example, the disk/corona model of Haardt & Maraschi (1993) has been successful at explaining the mean intrinsic slope for Seyfert galaxies of $\Gamma = 1.9$. However, Stern et al. (1995) have pointed out that this model has some difficulties in explaining a *range* of observed slopes and suggest a solution in which a number of distinct active regions illuminate the disk. Our data confirm the range of slopes observed by *Ginga*, and thus lend support to this hypothesis.

REFERENCES

Anders, E., & Grevesse, N. 1989, Geochim. Cosmochim. Acta, 53, 197
Antonucci, R. R., & Miller, J. S. 1985, ApJ, 297, 621
Arnaud, M., & Raymond, J. 1992, ApJ, 398, 394
Basko, M. M. 1978, ApJ, 223, 268
Bevington, P. R. 1969, Data Reduction and Error Analysis for the Physical Sciences (New York: McGraw-Hill)
Bond, I. A., & Matsuoka, M. 1993, MNRAS, 265, 619
Cappi, M., Mihara, T., Matsuoka, M., Hayashida, K., Weaver, K. A., & Otani, C. 1996, ApJ, 458, 149
Cash, W. 1979, ApJ, 228, 939
Dickey, J. M., & Lockman, F. J. 1990, ARA&A, 28, 215
Dotani, T., et al. 1995, *ASCA* News, 3
Edwards, A. W. F. 1972, Likelihood (Cambridge: Cambridge Univ. Press)
Elvis, M., Lockman, F. J., & Wilkes, B. 1989, AJ, 97, 777
Fabian, A. C., Nandra, K., Reynolds, C. S., Brandt, W. N., Otani, C., Tanaka, Y., Inoue, H., & Iwasawa, K. 1995, MNRAS, 277, L11
Fabian, A. C., Rees, M. J., Stella, L., & White, N. E. 1989, MNRAS, 238, 729
Fabian, A. C., et al. 1994, PASJ, 46, 59
Ford, H. C., et al. 1994, ApJ, 435, L27
Gendreau, K. 1995, Ph.D. thesis, Massachusetts Inst. of Technology
George, I. M., & Fabian, A. C. 1991, MNRAS, 249, 352
George, I. M., Turner, T. J., & Netzer, H. 1995, ApJ, 438, L67
George, I. M., et al. 1997, in preparation (Paper III)
Ghisellini, G., Haardt, F., & Matt, G. 1993, MNRAS, 267, 743
Guainazzi, M., Matsuoka, M., Piro, L., Mihara, T., & Yamauchi, M. 1994, ApJ, 436, L35
Guilbert, P. W., & Rees, M. J. 1988, MNRAS, 233, 475
Haardt, F., & Maraschi, L. 1993, ApJ, 413, 507
Hamann, F., & Ferland, G. J. 1993, ApJ, 418, 11
Krolik, J. H., & Kallman, T. R. 1987, ApJ, 329, L5
Krolik, J. H., Madau, P., & Zycki, P. 1993, ApJ, 420, L57
Laor, A. 1991, ApJ, 376, 90
Lampton, M., Margon, B., & Bowyer, S. 1976, ApJ, 208, 177
Leighly, K., Mushotzky, R. F., Yaqoob, T., Kuneida, H., Edelson, R. 1996, ApJ, 469, 147
Lightman, A. P., & White, T. R. 1988, ApJ, 335, 57
Maccacaro, T., et al. 1988, ApJ, 326, 680
Makishima, K. 1985, in The Physics of Accretion onto Compact Objects, ed. K. O. Mason, M. G. Watson, & N. E. White (Berlin: Springer), 250
Matt, G., Fabian, A. C., & Ross, R. R. 1993, MNRAS, 262, 179
Matt, G., Perola, G. C., & Piro, L. 1991, A&A, 245, 75
Matt, G., Perola, G. C., Piro, L., & Stella, L. 1992, A&A, 257, 63
McCall, M. L., Rybski, P. M., & Shields, G. A. 1985, ApJS, 57, 1
Mihara, T., Matsuoka, M., Mushotzky, R. F., Kunieda, H., Otani, C., Miyamoto, S., & Yamauchi, M. 1994, PASJ, 46, L137

Miyoshi, M., et al. 1995, Nature, 373, 127
Morrison, R., & McCammon, D. 1983, ApJ, 270, 119
Murphy, E. M., Lockman, F. J., Laor, A., & Elvis, M. 1996, ApJS, 105, 369
Mushotzky, R. F. 1982, ApJ, 256, 92
———. 1984, Adv. Space. Res., 3, 157
Mushotzky, R. F., Fabian, A. C., Iwasawa, K., Matsuoka, M., Nandra, K., & Tanaka, Y. 1995, MNRAS, 272, L9
Nandra, K., & George, I. M. 1994, MNRAS, 267, 974
Nandra, K., George, I. M., Mushotzky, R. F., Turner, T. J., & Yaqoob, T. 1997, ApJ, in press (Paper I)
Nandra, K., George, I. M., Turner, T. J., & Fukazawa, Y. 1996, ApJ, 464, 165
Nandra, K., & Pounds, K. A. 1994, MNRAS, 268, 405
Nandra, K., Pounds, K. A., Stewart, G. C., Fabian, A. C., & Rees, M. J. 1989, MNRAS, 236, 39P
Nousek, J. 1990, in Errors, Bias, and Uncertainties in Astronomy, ed. C. Jaschek & F. Murtagh (Cambridge: Cambridge Univ. Press), 167
Pogge, R. W. 1989, ApJ, 345, 730
Pounds, K. A., Nandra, K., Stewart, G. C., George, I. M., & Fabian, A. C. 1990, Nature, 344, 132
Ptak, A., Yaqoob, T., Serlemitsos, P. J., Mushotzky, R. F., & Otani, C. 1994, ApJ, 436, L31
Rees, M. J. 1984, ARA&A, 22, 471
Reynolds, C. S., Fabian, A. C., & Inoue, H. 1995a, MNRAS, 276, 1311
Reynolds, C. S., Fabian, A. C., Nandra, K., Inoue, H., Kunieda, H., & Iwasawa, K. 1995b, MNRAS, 277, 901
Ross, R. R., & Fabian, A. C. 1993, MNRAS, 261, 74
Shields, G. A., Skillman, E. D., & Kennicutt, R. C. 1991, ApJ, 371, 82
Stark, A. A., Gammie, C. F., Wilson, R. W., Bally, J., Linke, R. A., Heiles, C., & Hurwitz, M. 1992, ApJS, 79, 77
Stern, B. E., Poutanen, J., Svensson, R., Sikora, M., & Begelman, M. C. 1995, ApJ, 449, L13
Tanaka, Y., et al. 1995, Nature, 375, 659
Turner, M. J. L., et al. 1989, PASJ, 41, 345
Turner, T. J., & Pounds, K. A. 1989, MNRAS, 240, 833
Véron-Cetty, M.-P., & Véron, P. 1993, ESO Sci. Rep., 13, 1 (V93)
Warwick, R. S., Yaqoob, T., Pounds, K. A., Matsuoka, M., & Yamauchi, M. 1989, PASJ, 41, 721
Weaver, K. A., Nousek, J., Yaqoob, T., Hayashida, K., & Murakami, S. 1995, ApJ, 451, 147
Weaver, K. A., Yaqoob, T., Holt, S. S., Mushotzky, R. F., Matsuoka, M., & Yamauchi, M. 1994, ApJ, 436, 27
Yaqoob, T., Edelson, R. A., Weaver, K. A., Warwick, R. S., Mushotzky, R. F., Serlemitsos, P. J., & Holt, S. S. 1995, ApJ, 453, 81